University of Louisville

ThinkIR: The University of Louisville's Institutional Repository

12-2012

A unified picture of breaks and truncations in spiral galaxies from SDSS and S4G imaging.

Ignacio Martin-Navarro
Instituto de Astrofísica de Canarias

Judit Bakos
Instituto de Astrofísica de Canarias

Ignacio Trujillo
Instituto de Astrofísica de Canarias

Johan H. Knapen
Universidad de La Laguna

E. Athanassoula
Aix Marseille Universite

See next page for additional authors

Authors

Ignacio Martin-Navarro, Judit Bakos, Ignacio Trujillo, Johan H. Knapen, E. Athanassoula, A. Bosma, Sebastien Comeron, Bruce G. Elmegreen, Santiago Erroz-Ferrer, Dimitri A. Gadotti, Armando Gil de Paz, Joannah L. Hinz, Luis C. Ho, Benne W. Holwerda, Taehyun Kim, Jarkko Laine, Eija Laurikainen, Karin Menendez-Delmestre, Trisha Mizusawa, Juan Carlos Munoz-Mateos, Michael W. Regan, Heikki Salo, Mark Seibert, and Kartik Sheth

A unified picture of breaks and truncations in spiral galaxies from SDSS and S⁴G imaging

Ignacio Martín-Navarro,[1,2]⋆ Judit Bakos,[1,2] Ignacio Trujillo,[1,2] Johan H. Knapen,[1,2]
E. Athanassoula,[3] Albert Bosma,[3] Sébastien Comerón,[4] Bruce G. Elmegreen,[5]
Santiago Erroz-Ferrer,[1,2] Dimitri A. Gadotti,[6] Armando Gil de Paz,[7] Joannah L. Hinz,[8]
Luis C. Ho,[9] Benne W. Holwerda,[10] Taehyun Kim,[6,11,12] Jarkko Laine,[13]
Eija Laurikainen,[13] Karín Menéndez-Delmestre,[9] Trisha Mizusawa,[11,14,15]
Juan-Carlos Muñoz-Mateos,[11] Michael W. Regan,[16] Heikki Salo,[13] Mark Seibert[9]
and Kartik Sheth[11,14,15]

[1]*Instituto de Astrofísica de Canarias, E-38200 La Laguna, Tenerife, Spain*
[2]*Departamento de Astrofísica, Universidad de La Laguna, E-38205 La Laguna, Tenerife, Spain*
[3]*Laboratoire d'Astrophysique de Marseille (LAM), Marseille, France*
[4]*Korea Astronomy and Space Science Institute, 61-1 Hwaamdong, Yuseong-gu, Daejeon 305-348, Korea*
[5]*IBM T. J. Watson Research Center, PO Box 218, Yorktown Heights, NY 10598, USA*
[6]*European Southern Observatory, Casilla 19001, Santiago 19, Chile*
[7]*Departamento de Astrofísica, Universidad Complutense Madrid, Madrid, Spain*
[8]*University of Arizona, 933 N. Cherry Ave, Tucson, AZ 85721, USA*
[9]*The Observatories of the Carnegie Institution for Science, Pasadena, CA, USA*
[10]*European Space Agency, ESTEC, 2200 AG Noordwijk, the Netherlands*
[11]*National Radio Astronomy Observatory/NAASC, 520 Edgemont Road, Charlottesville, VA 22903, USA*
[12]*Astronomy Program, Department of Physics and Astronomy, Seoul National University, Seoul 151-742, Korea*
[13]*Division of Astronomy, Department of Physical Sciences, University of Oulu, Oulu, FIN-90014, Finland*
[14]*Spitzer Science Center, 1200 East California Boulevard, Pasadena, CA 91125, USA*
[15]*California Institute of Technology, 1200 East California Boulevard, Pasadena, CA 91125, USA*
[16]*Space Telescope Science Institute, Baltimore, MD, USA*

ABSTRACT

The mechanism causing breaks in the radial surface-brightness distribution of spiral galaxies is not yet well known. Despite theoretical efforts, there is not a unique explanation for these features and the observational results are not conclusive. In an attempt to address this problem, we have selected a sample of 34 highly inclined spiral galaxies present in both the Sloan Digital Sky Survey (SDSS) and the *Spitzer* Survey of Stellar Structure in Galaxies (S⁴G). We have measured the surface-brightness profiles in the five Sloan optical bands and in the 3.6-μm *Spitzer* band. We have also calculated the colour and stellar surface mass density profiles using the available photometric information, finding two differentiated features: an innermost *break radius* at distances of $\sim 8 \pm 1$ kpc [$0.77 \pm 0.06 R_{25}$] and a second characteristic radius, or *truncation radius*, close to the outermost optical extent ($\sim 14 \pm 2$ kpc [$1.09 \pm 0.05 R_{25}$]) of the galaxy. We propose in this work that breaks might be phenomena related to a threshold in the star formation, while truncations are more likely a real drop in the stellar mass density of the disc associated with the maximum angular momentum of the stars.

Key words: galaxies: formation – galaxies: fundamental parameters – galaxies: photometry – galaxies: spiral – galaxies: structure.

1 INTRODUCTION

The vast majority of spiral galaxies do not follow a radial surface-brightness decline mimicking a perfect exponential law, as proposed

⋆E-mail: imartin@iac.es

by Patterson (1940), de Vaucouleurs (1958) and Freeman (1970). Depending on the shape of the surface-brightness distribution, a classification for face-on galaxies has been developed by Erwin, Beckman & Pohlen (2005) and Pohlen & Trujillo (2006). It distinguishes three different types of profiles. Type I (TI) is the classical case, with a single exponential describing the entire profile; Type II (TII) profiles have a downbending brightness beyond the break. Type III (TIII) profiles are characterized by an upbending brightness beyond the break radius. Relative frequencies for each type are 10 per cent, 60 per cent and 30 per cent (Pohlen & Trujillo 2006) in the case of late-type spirals.

Photometric studies of TII galaxies reveal that the radial scalelength of the surface-brightness profiles changes when a characteristic radius ($\sim$10 kpc) is reached. This so-called break radius is described in several studies of face-on galaxies (Erwin et al. 2005; Pohlen & Trujillo 2006; Erwin, Pohlen & Beckman 2008) and is also found if galaxies are observed in edge-on projections (van der Kruit & Searle 1982; de Grijs, Kregel & Wesson 2001; van der Kruit 2007). Using faint-magnitude stars, Ferguson et al. (2007) also found a break in the surface-brightness profile of M33. In contrast, no break was detected by star-counting in either NGC 300 (Bland-Hawthorn et al. 2005; Vlajić, Bland-Hawthorn & Freeman 2009) or NGC 7793 (Vlajić, Bland-Hawthorn & Freeman 2011). Works on galaxies beyond the nearby Universe (Pérez 2004; Trujillo & Pohlen 2005; Azzollini, Trujillo & Beckman 2008) show the presence of a break at redshifts up to $z \sim 1$. These results suggest that breaks, once formed, must have been stable for the last 8 Gyr of galaxy evolution. Cosmological simulations (Governato et al. 2007; Martínez-Serrano et al. 2009) support the idea of a break in the light distribution of disc galaxies as well.

Different mechanisms explaining the origin of TII breaks have been proposed. All these theories can be sorted into two families. A possible scenario is that the break could be located at a position where a threshold in the star formation occurs (Fall & Efstathiou 1980; Kennicutt 1989; Elmegreen & Parravano 1994; Schaye 2004; Elmegreen & Hunter 2006). A change in the stellar population would thus be expected at the break radius, but not necessarily a downbending of the surface mass density profile as shown by some simulations (Sánchez-Blázquez et al. 2009; Martínez-Serrano et al. 2009). Supporting this, Bakos, Trujillo & Pohlen (2008) found that in a sample of 85 face-on galaxies (see Pohlen & Trujillo 2006), the $(g' - r')$ Sloan Digital Sky Survey (SDSS) colour profile of the TII galaxies is, in general, U-shaped, with a minimum at the break radius, also hinting at a minimum in the mean age of the stellar population at the break radius. This is in agreement with studies on resolved stellar populations across the break (de Jong et al. 2007; Radburn-Smith et al. 2012). Furthermore, the surface mass density profile recovered from the photometry shows a much smoother behaviour, in which the break is almost absent compared with the surface-brightness profile. Numerical simulations (Debattista et al. 2006; Roškar et al. 2008; Sánchez-Blázquez et al. 2009; Martínez-Serrano et al. 2009) reveal how the secular redistribution of the angular momentum through stellar migration can drive the formation of a break. In the papers of Roškar et al. (2008) and Sánchez-Blázquez et al. (2009), a minimum in the age of the stellar population is found at the break radius, in agreement with the results of Bakos et al. (2008). It is also remarkable that the mean break radius in the simulations of Roškar et al. (2008) is very close ($2.6\,h_{\rm r}$) to the observational result ($2.5 \pm 0.6\,h_{\rm r}$) measured by Pohlen & Trujillo (2006), where the values are given in radial scalelength units ($h_{\rm r}$). However, van der Kruit & Searle (1982) showed that the Goldreich–Lynden–Bell criterion for stability of gas layers

offered a poor prediction for the truncation radius in their sample of edge-on galaxies. Focusing on these high inclined galaxies, van der Kruit (1987, 1988) proposed an alternative scenario where the break could be related to the maximum angular momentum of the protogalactic cloud, leading to a break radius of around four or five times the radial scalelength. This mechanism would also lead to a fast drop in the density of stars beyond the break. Observations of edge-on galaxies, such as those by van der Kruit & Searle (1982), Barteldrees & Dettmar (1994) or Kregel, van der Kruit & de Grijs (2002), place the break at a radius around four times the radial scalelength, supporting this second explanation.

There is a clear discrepancy between the positions of the breaks located in the face-on view compared with those breaks found in the edge-on perspective. In the face-on view, the breaks are located at closer radial distances to the centre than in the edge-on cases. Are the two types of breaks the same phenomenon? On the one hand, edge-on observations tend to support the idea of maximum angular momentum as the main actor in the break formation. On the other hand, face-on galaxies, supported by numerical simulations, favour a scenario where the break is associated with some kind of threshold in the star formation along the disc. Only a few studies have attempted to give a more global vision of the problem (Pohlen et al. 2004, 2007) by deprojecting edge-on surface-brightness profiles. Pohlen et al. (2007) and Comerón et al. (2012) found that the classification explained at the beginning of the current paper, consisting of TI, TII and TIII profiles, is basically independent of the geometry of the problem. Consequently, the difference between the break radius obtained from edge-on galaxies and the one from face-on galaxies cannot be related to the different inclination angle. More details on the current understanding of breaks and truncations can be found in the recent review by van der Kruit & Freeman (2011, section 3.8).

Despite the fact that truncations in edge-on galaxies and breaks in face-on galaxies have traditionally been considered equivalent features, our aim in the current paper is to understand the already-noted observational differences, proposing a global and self-consistent understanding of the breaks. We use images in six different filters (five SDSS bands and the *Spitzer* Survey of Stellar Structure in Galaxies (S^{4}G) 3.6-μm band) to study the radial surface-brightness distribution in a sample of 34 edge-on galaxies. We also measure the colour and the stellar surface mass density profiles for each object, trying to constrain the most plausible mechanism for break formation.

The layout of this work is as follows. In Section 2 the characteristics of the sample are presented. Section 3 describes how the profiles are measured. The analysis is shown in Section 4 and then we discuss the results in Section 5. The main conclusions listed in Section 6. Tables referenced in the paper are in Appendix A.

Throughout, we adopt a standard ΛCDM set of cosmological parameters ($H_0 = 70\,{\rm km\,s^{-1}\,Mpc^{-1}}$; $\Omega_{\rm M} = 0.30$; $\Omega_\Lambda = 0.70$) to calculate the redshift-dependent quantities. We have used AB magnitudes unless otherwise stated.

2 SAMPLE AND DATA

Our sample of galaxies has been selected to cover edge-on objects present in both the Sloan Digital SDSS Data Release 7 (Abazajian et al. 2009) and the S^{4}G (Sheth et al. 2010). We find 49 highly inclined (inclination $\gtrsim$88°) objects satisfying this criterion. In this sense our sample is neither volume-limited nor flux-limited.

For each object, the morphological type, the corrected *B*-band absolute magnitude (M_B) and the maximum velocity of the rotation

curve were obtained from the HyperLeda data base (Paturel et al. 2003). Using the NASA/IPAC Extragalactic Data base (NED: Helou et al. 1991), we obtained most distances from primary indicators, except for three cases (PGC 029466, UGC 5347 and UGC 9345) for which the distance was obtained using the redshift.

Finally, from the original 49 galaxies, we keep only those objects brighter than $M_B = -17$ mag and with morphological type Sc or later. Table A1 summarizes the general information available for each galaxy in the final sample. We focus our studies on late-type spiral galaxies. These late Hubble types are known to have the most quiescent evolution during cosmic time, hence the fossil records imprinted by early galaxy formation and evolution processes likely survive to the present day.

2.1 SDSS data

For all the galaxies in the sample, the SDSS data were downloaded in all five available bands $\{u', g', r', i', z'\}$. SDSS observations are stored in the format of 2048×1489 pixel ($\sim 13.51 \times 9.83$ arcmin^2) frames that cover the same piece of sky in all bands. These frames are bias-subtracted, flat-fielded and purged of bright stars, but still contain the sky background. These frames might not be large enough to contain extended objects completely. For this reason, to assemble mosaics that are large enough to study extended objects we needed to download several adjacent frames from the SDSS archive. We estimate the sky background of these frames independently (see Section 2.2.1 for a more detailed description) and then we assemble the final mosaics in all five bands, centred on the target galaxy, by using SWARP (Bertin et al. 2002).

The pixel size in the SDSS survey is 0.396 arcsec and the exposure time is ~ 54 s. From this, we calculated the surface brightness in the AB system as

$$\mu_{\text{SDSS}} = -2.5 \times \log (counts) + ZP,$$
$$ZP = -2.5 \times 0.4 \times (aa + kk + airmass)$$
$$+ 2.5 \times \log (53.907456 \times 0.396^2),$$

where *aa*, *kk* and *airmass* are the photometric zero-point, the extinction term and the airmass, respectively. These parameters are stored in the header of each SDSS image.

2.2 S⁴G data

The S⁴G project is a survey of a representative sample of nearby Universe galaxies ($D < 40$ Mpc) that collects images of more than 2000 galaxies with the *Spitzer* Infrared Array Camera (IRAC: Fazio et al. 2004). In particular, we are interested in the 3.6-µm band (channel 1), which is less affected by dust than the SDSS optical bands and is a good tracer for stellar mass in our galaxies. The fact that the optical depth in this band is lower than in the SDSS images is crucial as we are dealing with edge-on objects, with a lot of dust along the line of sight. The IRAC 3.6-µm images were reduced by the S⁴G team. They have a pixel scale of 0.75 arcsec pixel^{-1} and the spatial resolution is ~ 100 pc at the median distance of the survey volume. Also, the azimuthally averaged surface-brightness profile typically traces isophotes down to a (1σ) surface-brightness limit ~ 27 mag arcsec^{-2} (see Sheth et al. 2010). The conversion to AB surface magnitudes is given by

$$\mu_{\text{S}^4\text{G}} = -2.5 \times \log (counts) + 20.472.$$

3 DATA HANDLING AND RESULTS

3.1 Data handling

3.1.1 Sky subtraction

Since the breaks are expected to happen at low surface brightness (a typical value of ~ 24 mag arcsec^{-2} in the SDSS g' band was found by Pohlen & Trujillo 2006, for face-on galaxies), a very careful sky estimation is needed to obtain reliable results. In this context, working with data taken with different instruments at different wavelengths requires a different treatment for the SDSS and S⁴G data.

In the case of the SDSS images, after removing the 1000 counts of the SOFTBIAS added to all SDSS chips, we measure the fluxes in about ten thousand randomly placed five-pixel-wide apertures. We apply a resistant mean[1] to the distribution of the aperture fluxes, and carry out several iterations to get rid of the fluxes biased by stars and other background objects. The mean of the bias-free distribution provides accurate measurement of the sky background and is then subtracted from the chips.

For the S⁴G data, the sky treatment was completely different because of the presence of important gradients across the images (see Comerón et al. 2011). The adopted strategy was to mask every object in the image and then make a low-order polynomial fit of the background in the same way that Comerón et al. (2011) did in their study of NGC 4244. In order to establish a threshold between sky/non-sky pixels, we built the histogram of the image and, with the assumption that this histogram is dominated by the sky pixels, we calculated the maximum and the full width at half-maximum (FWHM) of this distribution. The FWHM measured in that way can be associated with an effective sigma (σ_e) that we supposed to be representative of the standard deviation of the background. After this, we performed five two-dimensional fits with five different polynomial orders ($\mathcal{O} = \{0, 1, 2, 3, 4\}$), including only those pixels with a value between the maximum of the histogram $\pm 3\sigma_e$. The outcome of this stage was five sky-subtracted images, each one derived from one of the fits. The difference between these images was used (see Section 3.1.2) to establish the surface-brightness limit in the 3.6-µm surface-brightness profile. In Fig. 1 we show a raw S⁴G image (left) where the gradients across the image are obvious, the mask image (centre) with the pixels used to fit the background represented in white and, as an example, the third-order sky-subtracted image (right).

3.1.2 Estimating the position angle of the slit

Our aim is to extract surface-brightness profiles along the disc in a slit that represents the same physical distance (1.2 kpc) vertically in all galaxies. For this reason, this slit has to be aligned accurately with the disc of our galaxies. The position angle (PA) was defined as the angle that maximizes the total number of non-sky pixels within the previously fixed slit. This definition is consistent with the idea followed in the surface-brightness profile calculation. The measurement will be robust if the size of the galaxy is large enough compared with the field of view. As in Section 2.2.1, we distinguished sky pixels from non-sky pixels, setting them to 0 and 1 respectively. We rotated the image by a certain angular step and

---

[1] The resistant mean trims away outliers using the median and the median absolute deviation. It is implemented as an INTERACTIVE DATA LANGUAGE (IDL) routine.
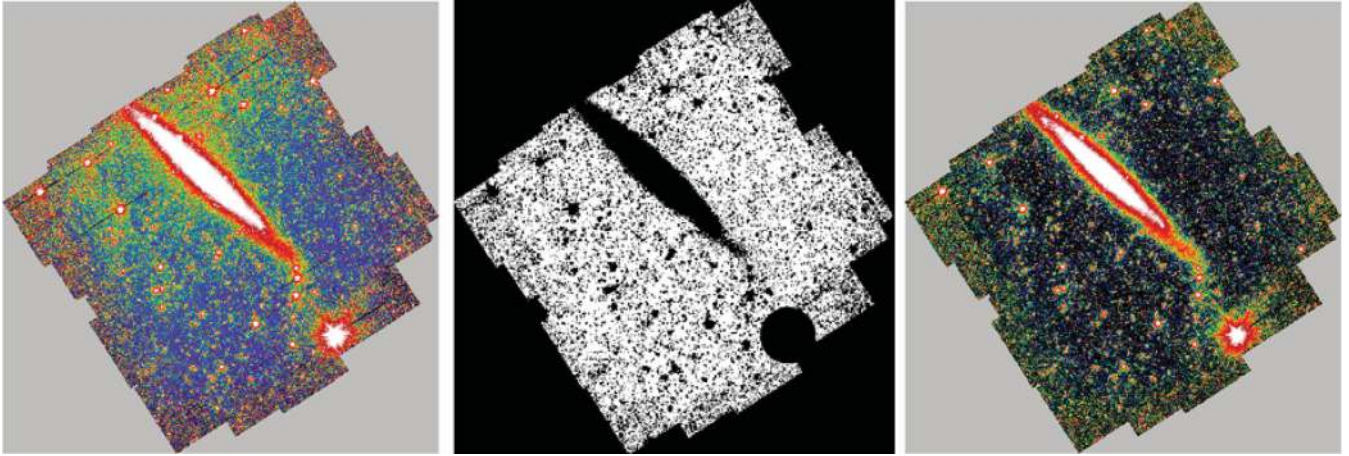
Figure 1. Sky-subtraction steps for NGC 4244 (3.6-µm band). From left to right: (1) original image, (2) image mask where white pixels are those used to estimate the background shape, (3) image after the subtraction of one of the polynomial fittings (third order).
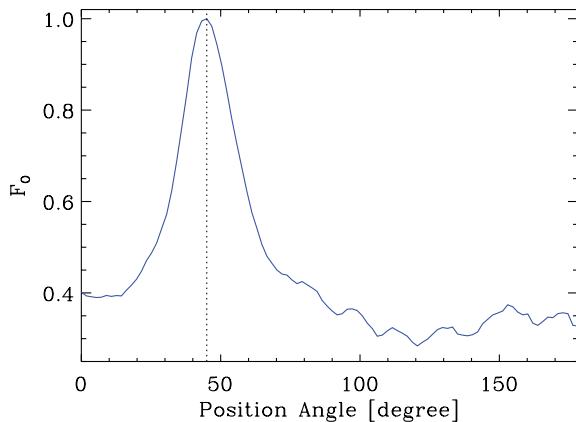

Figure 2. The fraction of non-background pixels within the slit aperture (F_O) as a function of the position angle of the slit for NGC 4244 (r' band). The vertical dashed line marks the centre of the angular interval used to refine the measurement of the final PA.

then summed the value of all the pixels within the slit. The desired angle corresponds to the maximum of this distribution.

In order to obtain the PA with enough accuracy, but with an acceptable computational cost, the process was divided into two phases. In the first one, a low-resolution profile was obtained by rotating the galaxy between $0°$ and $180°$ in 100 consecutive steps. We then defined an angular interval around the maximum of the resulting low-resolution profile and used a high-resolution step of $0°.2$. The maximum found in this second phase is the PA of the galaxy. Fig. 2 shows the normalized fraction of flux within the aperture versus the slit position-angle profile for the case of NGC 4244, with a peaked distribution around the maximum (PA = $47°.2$).

As the Galactic plane is expected to be dust-attenuated, we employed the 3.6-µm S^4G images to calculate the PA. The PA derived from the SDSS data was in all cases compatible with the S^4G measurements, taking into account the associated errors. In addition, we repeated the measurement of the PA, changing the threshold used to distinguish the sky pixels, taking at the end the average of the resulting values.

The PA calculated in this way is intuitive but is sensitive to the presence of extended objects in the field and to asymmetries in the light distribution of the galaxy. For that reason, we had to manually set the PA in seven cases to align the Galactic plane completely

with the slit, with a typical deviation with respect to the automatic measurement $\langle PA_{final} - PA_{auto} \rangle = 0.5 \pm 0°.1$. The PA calculated here is compared in Table A2 with the position angle from HyperLeda[2] for each galaxy in the sample, showing a mean difference between our measurements and the PA from HyperLeda of $\sim 0°.7$. It is worth noting here that the PA given by HyperLeda is the result of averaging all entries in the data base for each object, sometimes with very different values (e.g. for NGC 4244, the HyperLeda PA ($42°.2$) is the average of four significantly different measurements: $48°$, $48°$, $27°$ and $45°.2$).

3.1.3 Image masking

To study the outskirts of galaxies with the desired precision it was necessary to mask objects that clearly do not belong to the galaxy (foreground stars, background galaxies). This masking process allowed us to obtain cleaner surface-brightness profiles and also to avoid contamination of the faintest parts by external objects.

For the S^4G images, the masks were supplied by the $S4G$ team and are described in Sheth et al. (2010). In the case of the SDSS images, we generated the masks using the package SEXTRACTOR (Bertin & Arnouts 1996). Background objects and foreground stars were detected using a master image composed of all five SDSS bands, scaled to the r'-band flux. Then, oversized elliptical masks were placed on to the detected sources using SEXTRACTOR parameters such as measured flux, elongation, etc. To increase the accuracy in this process, the masking was done in two consecutive steps. In the the first one, the bigger and brighter background objects were masked. In the second step, we performed a more detailed detection process to mask any possible remaining object in the field. By doing this, we could successfully mask background objects within a wide range of sizes.

3.2 Surface-brightness profiles

To extract the profile along the radial distance of the galaxies, a slit of constant physical width is placed over the Galactic Plane and then used to calculate how the flux varies along the slit. The width of

---

[2] By definition, the PA increases (from $0°$ to $180°$) from the north to the east, i.e. counterclockwise.
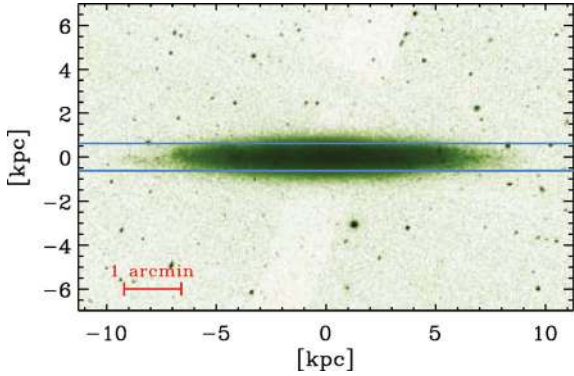
Figure 3. The galaxy NGC 5023 is shown with the region (slit) used to calculate the surface-brightness profile delimited by the solid lines (blue in the online article).

Figure 4. Surface-brightness profile for the galaxies NGC 5907 (upper panel) and NGC 4244 (bottom panel) in the r' band. The mean profile is shown by filled circles (blue in the online article), whereas left and right profiles are represented by diamonds (red and yellow in the online article, respectively).

the slit was fixed to 1.2 kpc following the assumption of a vertical scalelength equal to 0.6 kpc (Kregel et al. 2002). For illustrative purposes, in Fig. 3 the slit position (in blue in the online article) is shown over the r'-band image of NGC 5023.

In general, the process to obtain the surface-brightness profiles was the same for the SDSS and for the S⁴G data. The first step was to divide the slit along the major axis into cells of 0.3 arcsec radial width. The averaged value of the flux within each cell was calculated using a 3σ rejection mean. This first stage yields a crude estimate of the surface-brightness profile. The centre of the galaxy was supposed to correspond to the brightest cell of this profile and, to avoid any kind of misalignment between the different filters, we took the right ascension and declination of the S⁴G brightest cell as the centre in all the other profiles. The sky was again measured on the left and right sides of the galaxies in order to, later, remove any possible residual contribution after the initial sky subtraction (Section 2.2.1).

After that, we calculated the *right* and *left* surface-brightness profiles, with the size of the bins linearly increasing with a factor 1.03 between consecutive cells to improve the signal-to-noise ratio in the outskirts of the galaxies. The right/left residual sky value measured at the beginning of the process was also subtracted for the right/left profiles to obtain the final surface-brightness distributions. The surface brightnesses of these residual sky corrections were typically ∼30 mag arcsec⁻² for the g' band and ∼29 mag arcsec⁻² for the 3.6-μm band.

Finally, a mean profile was constructed as the average of the left and right profiles. These averaged profiles are the ones used in this study. Looking at the individual right/left profiles of all our sample, it was clear that in some cases (e.g. NGC 4244) there are considerable asymmetries (up to 0.8 r' mag arcsec⁻² difference between the averaged profile and the right/left profiles at $r = 550$ arcsec for that object) but, as we wanted to explore the surface-brightness profiles down to very faint regions, the combination of the two sides of the galaxies is necessary. As an example, in Fig. 4 we represent the mean, left and right surface-brightness profiles in the SDSS r' band for a symmetric case (NGC 5907) in opposition to the more asymmetric galaxy NGC 4244.

Beyond a certain radius, the sky subtraction becomes a dominant factor in determining surface-brightness profiles. Having used different sky-subtraction techniques, the maximum radial extension of a reliable surface-brightness profile needs to be measured separately for the SDSS and for the S⁴G data.
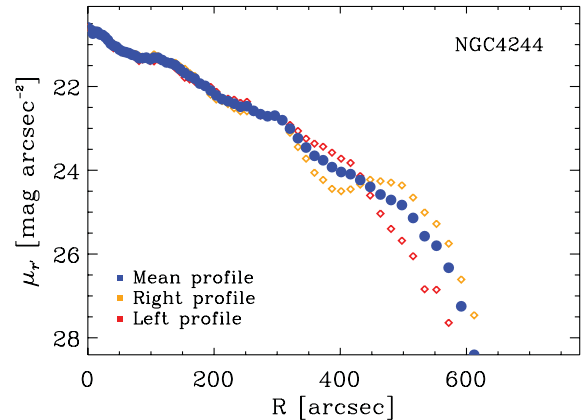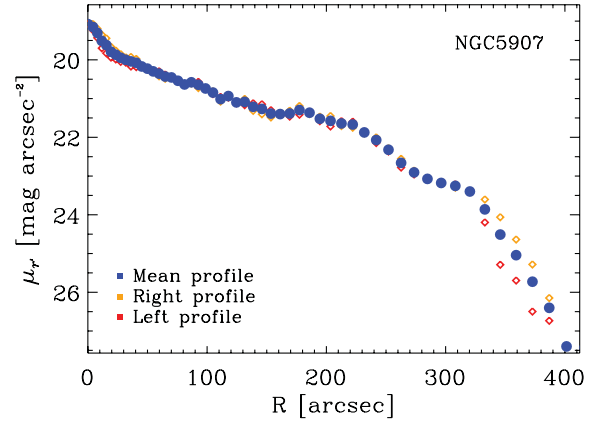
3.2.1 SDSS surface-brightness limit

To estimate how faint we can explore the SDSS profiles, we defined a certain critical surface magnitude (μ_{crit}) that sets the limit for our profiles. Following Pohlen & Trujillo (2006), we defined μ_{crit} as the surface brightness where the two profiles obtained by under/oversubtracting the sky by $-1/+1\,\sigma_{\mathrm{sky}}$ start to differ by more than 0.2 mag arcsec⁻², where σ_{sky} is given by

$$\sigma^2_{\mathrm{sky}} = \sigma^2_{\mathrm{sky,\ left}} + \sigma^2_{\mathrm{sky,\ right}},$$

with $\sigma_{\mathrm{sky,\ left}}$ and $\sigma_{\mathrm{sky,\ right}}$ the standard deviation of the residual sky measured on the left and right sides of the galaxy. On average, we could reach a surface-brightness magnitude limit equal to 26.1 ± 0.1 mag arcsec⁻² in the SDSS r' band. This value is a characteristic limit for the g', r' and i' SDSS data, with the remaining SDSS images being typically shallower (e.g. $\langle \mu_{u',\mathrm{lim}} \rangle = 25.7$ mag arcsec⁻²; $\langle \mu_{z',\mathrm{lim}} \rangle = 24.2$ mag arcsec⁻²).

3.2.2 S⁴G surface-brightness limit

The limit for the S⁴G data had to be more strictly defined because of the presence of gradients across the S⁴G images. As discussed in Section 2.2.1, we have, for each object, five images from five different polynomial fits to the background. The limit was established

where the function

$$\mu_{\mathrm{crit}} = \frac{1}{5} \sum_{n=0,..,4} |\mu_n - \langle \mu \rangle|$$

became greater than 0.2 mag arcsec^{-2}. In other words, the limit for the S^{4}G profiles was placed where the mean difference between the five profiles and the mean one was greater than 0.2 mag arcsec^{-2}. A typical value of 26.1 ± 0.2 mag arcsec^{-2} was found for this limit in the S^{4}G 3.6-μm band.

The limit defined in this way is not necessarily the same for the left and right sides of a galaxy. The mean profile is in fact the average of two profiles until the surface magnitude limit of the 'shallower' side. Beyond that, the mean profile is only that of the 'deeper' side of the galaxy.

3.3 Colour profiles

From the surface-brightness profiles one can directly obtain the radial colour profiles of an object. However, the interpretation of the edge-on colour profiles is not straightforward. On the one hand, the presence of dust in the Galactic plane will generate redder colours and change the actual shape of the colour profile compared with that expected in its absence. On the other hand, effects related to edge-on projection (integration of light from different radii along the line of sight and a bigger optical depth because of the presence of dust) are difficult to handle and to account for in an edge-on colour profile.

In this work, we have focused only on those profiles that could reach the lowest surface-brightness values (i.e. the colour profiles derived from the deepest surface-brightness profiles). In particular, we calculated for each galaxy the $(g' - r')$, $(r' - i')$ and $(r' - 3.6\text{-}μm)$ colour profiles.

3.4 Stellar surface mass density profiles

The final quantity that we obtained from the images is the stellar surface mass density (Σ_λ). We can relate Σ_λ to the surface brightness at a certain wavelength (μ_λ) and to the mass-to-luminosity ratio $(M/L)_\lambda$ at that given λ (see Bakos et al. 2008) using the following expression:

$$\log \Sigma_\lambda = \log(M/L)_\lambda - 0.4(\mu_\lambda - m_{\mathrm{abs}\,\odot,\lambda}) + 8.629,$$

where Σ_λ is given in M$_\odot$ pc^{-2}. Having $\mu_{r'}$ from the photometry, one just needs to know the value $(M/L)_{r'}$ along the galaxy to obtain the Σ_λ profile. We used the relation proposed by Bell et al. (2003) to estimate $(M/L)_{r'}$ as follows:

$$\log(M/L)_{r'} = [a_{r'} + b_{r'} \times (g' - r')] - 0.15,$$

where $a_{r'}$ and $b_{r'}$ are -0.306 and 1.097 respectively. We then have the stellar surface mass density as a function of all known variables.

As mentioned in Section 3.2, the interpretation of edge-on colour profile is not as direct as in the face-on case. Dust attenuation and error propagation in this kind of profile are very important and thus one has to be aware of all these effects while interpreting the surface mass density profiles.

3.5 Presentation of the results

Below, briefly, we will show some examples of the profiles extracted in this work. For the rest of the galaxies, we refer the reader to Appendix B. The upper left panels in these figures show the six-band surface-brightness profiles used in this paper. The dashed

vertical lines mark those radii where a change in the exponential behaviour happens, defined as described in Section 4.3.

On the bottom left panel we represent the colour profiles. The colour profiles are shown down to the distance where data points have an error less than or equal to 0.2 mag, with the error calculated as the quadratic sum of the errors in the individual surface-brightness profiles.

The bottom right panel is occupied by a g'-band image of the galaxy, with vertical lines marking the characteristic radii, in the same way as in the surface-brightness profiles. The angular distance from the centre of the galaxy to those lines is shown at the top of the image.

Finally, the upper right panel shows the stellar surface mass density profile. In the same panel is overplotted the 3.6 μm surface-brightness profile, which is expected to be a good tracer of the stellar mass density. In this panel we have not limited the extent of the profiles and therefore the farthest points have to be considered with caution.

4 ANALYSIS

4.1 Break radius and scalelengths

In order to quantify the radial distance where the change in exponential scalelength occurs, we have linearly fitted the r'-band averaged surface-brightness profile of each galaxy. We have visually selected all the disc regions showing a differentiated exponential behaviour and have then made an independent linear fit over each one of those regions. The characteristic radius where the exponential scalelength changes is set at the intersection point between two straight lines derived from the fit of two adjacent regions. Fig. 5 shows, as an example, the fit for UGC 06862. The black dashed lines represent the linear fit of each part of the disc. The dotted line (red in the online article) marks the intersection point between the two fits. Table A3 lists the regions of the disc where the fits were made for each individual galaxy. In addition, Table A4 lists where all characteristic radii occur in each galaxy in the sample.

Apart from identifying different characteristic radii, we have measured r_{max} as the radial distance at which a hint of a new change in the exponential behaviour is present, but there were not enough points to perform a reliable fit because it occurs at a surface magnitude
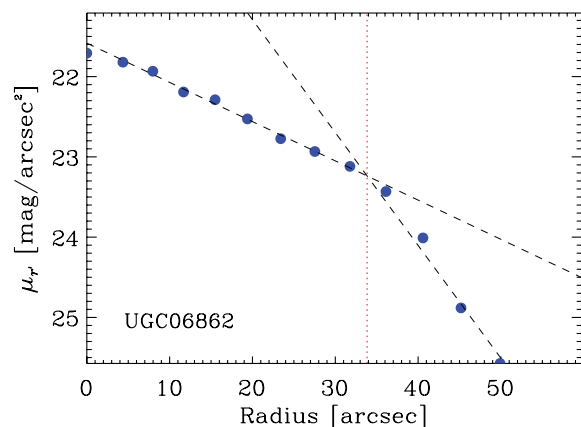

Figure 5. Fit of the r'-band surface-brightness profile of UGC 06862. The fit of the two characteristic regions is shown as a black dashed line, while the radius where the change in the slope occurs is marked with a dotted line (red in the online article). We have defined this radius as the intersection point between the two linear fits.

too close to the surface-brightness limit. If no such hint is detected, r_{max} then represents a lower limit for a potential new characteristic radius detection.

4.2 Overall behaviour

To exemplify the findings of our work, we will focus on the interpretation of those objects that, in particular, better reflect the general behaviour of the surface-brightness profiles of our sample. In any case, the same information is available for all the galaxies in Appendix B.

A paradigmatic example of the behaviour found in the surface-brightness profiles is found in NGC 4244 (Fig. 6). In the inner parts of the galaxy, the shape of the surface-brightness profile is dominated by an exponential decline but, reaching a break radius $r \sim 290$ arcsec (vertical line in Fig. 6, red in the online article), the slope becomes more pronounced. If we keep moving farther away, we find a second change in the exponential behaviour (vertical line, blue in the online article) happening at $r \sim 550$ arcsec. In the image of the galaxy shown in the bottom right panel, we can see how the first break radius (inner lines) marks an inner disc, while the second break radius is very close to the visual edge of the galaxy for this exposure. It is worth noting here that the asym-

metry of the brightness distribution in this object (see Section 3.1) makes the break radii different for the two sides of the galaxy. This has already been noticed in several studies (de Jong et al. 2007; Comerón et al. 2011; Holwerda et al. 2012). While Holwerda et al. (2012) noted a bright star-forming knot on either side of this galaxy but at slightly different radii, Comerón et al. (2011) stated that this asymmetry 'can be explained by a combination of the galaxy not being perfectly edge-on and a certain degree of opacity of the disc'. de Jong et al. (2007) proposed this asymmetry as the cause of the difference between their measurements for the break radial distance of the 'shorter' galactic side and the results of van der Kruit & Searle (1981) and Fry et al. (1999), who placed the break radius at around 570 arcsec as a consequence of averaging both sides of the galaxy. It is worth noting that this asymmetry makes the breaks smoother than in the case of more symmetric galaxies.

Lastly, in the stellar surface mass density plot, the second radius is associated with a steeper drop in both profiles than the first break, which has only a minor feature in Fig. 6 like that in the surface-brightness profiles.

Another representative example (in this case a symmetric galaxy) is NGC 5907 (Fig. 7). The surface-brightness profiles resemble a typical TII, with the inner break around 240 arcsec. As in the case
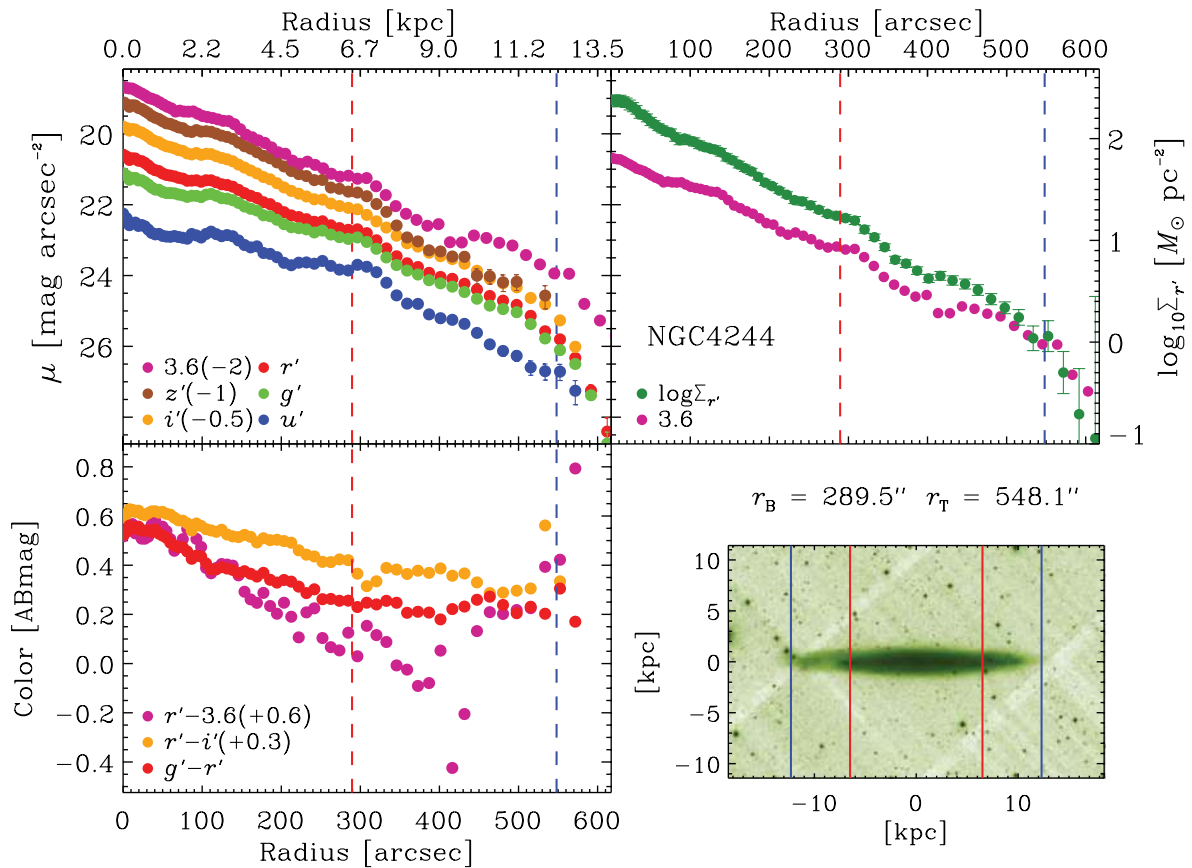

Figure 6. Surface brightness, colour and stellar surface mass density profiles of NGC 4244. The upper left panel shows six surface-brightness profiles from the different photometric bands used in the current paper. Dashed vertical lines mark where a change in the exponential behaviour happens. On the upper right panel the stellar surface mass density profile and the 3.6-μm surface-brightness profile are simultaneously plotted. The bottom left panel shows the three deeper colour profiles from the available photometric bands. Lastly, the bottom right panel is occupied by a g'-band image of the galaxy. For this object the surface-brightness distribution shows two clearly differentiated regions: one inner region before the left line (red in the online article) and a second outer region after the right line (blue in the online article). The position of the two breaks is shown in the bottom right panel. The last characteristic radius is near to the visible edge of the galaxy and it is reflected as a drop in the stellar surface mass density profile. On the other hand, the first break is clearly within the galactic disc and does not seem to affect the behaviour of the mass distribution dramatically.
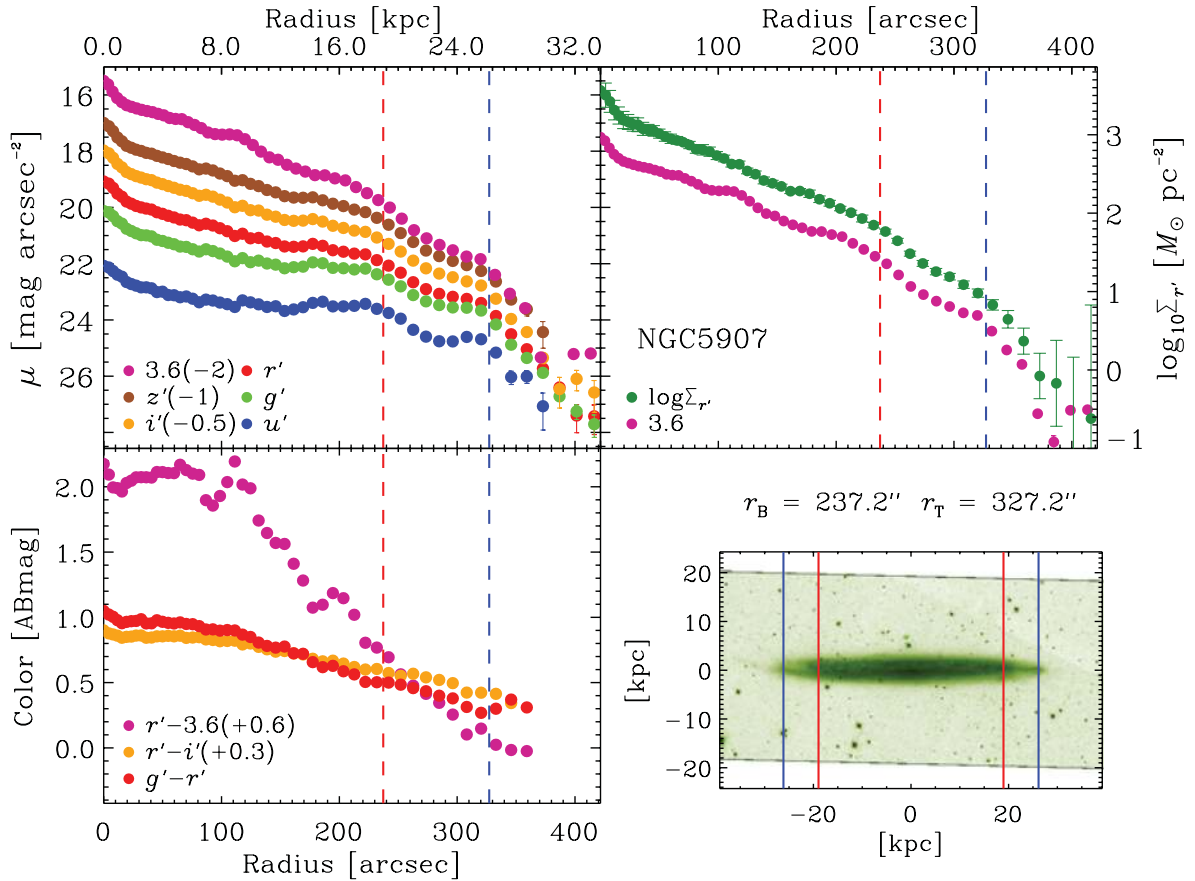
Figure 7. As in Fig. 6, but now for NGC 5907. The first break radius is placed at around 240 arcsec. The further break radius can be found at ~330 arcsec. In contrast to what we observe in NGC 4244, there is a big difference between the values of the optical colour profiles and the $(r' - 3.6\,\mu\text{m})$ colour profile that could be related to a stronger dust attenuation of the inner parts of this galaxy compared with NGC 4244.

of NGC 4244, there is a second change in the exponential behaviour at a radius $r \sim 330$ arcsec.

A clear difference from NGC 4244 are the high values of the $(r' - 3.6\,\mu\text{m})$ colour in the central region of the galaxy. Knowing that the IR band is less sensitive to dust attenuation, this red value of the $(r' - 3.6\,\mu\text{m})$ colour could be explained by the attenuation of dust in the optical bands. This is a very common behaviour among our sample of galaxies, since it is clearly present in at least 12 objects (see Appendix B). Paying attention to the stellar surface mass density plot, one can see again how the change in the slope is much pronounced at the second break radius compared with the change at the inner break radius. This time, since the galaxy is very symmetric, this change is clearly visible.

4.3 Feature classification

Many of our galaxies (18 out of 34) show two break radii in their profiles. The characteristics of the breaks seems to be different (see Section 4.2) depending on whether they are in the inner or the outer regions of the disc. For this reason we attempt to establish an observational classification for these features. Assuming that both breaks have a different physical origin, we have studied their characteristics in those cases when it was easy to distinguish one type from the other, i.e. when both breaks appear simultaneously in the same galaxy. Having characterized the type of break, this allowed us to extend the classification to those galaxies where only one break was present in the surface-brightness profile.

We labelled the first radius as the break radius (r_B) and the second radius as the truncation radius (r_T). In order to define an empirical criterion, we have investigated the distributions of these breaks and truncations as a function of two different parameters: h_0/h_feature (with h_0 the innermost scalelength and h_feature the scalelength after the break (h_B) or the truncation (h_T)) and $r_\text{feature}/h_\text{feature}$ (with r_feature representing r_B or r_T, i.e. the radial distance from the galactic centre to the break or the truncation position). The meaning of each parameter is exemplified in Fig. 8.

Fig. 9 shows the histograms for the breaks and truncation versus each one of the above-defined ratios, measured in the SDSS r'-band surface-brightness profiles. In the online figure, the break distribution is shown in red while the truncations are represented by a blue histogram. It is clear from Fig. 9 that breaks and truncations are partially degenerate when using the h_0/h_feature parameter but both characteristic radii are fully differentiated using the $r_\text{feature}/h_\text{feature}$ parameter. We find $r_\text{feature}/h_\text{feature} = 5$ as a typical value defining the break-truncation boundary.

We define, then, a break in the surface-brightness profile as a slope change (from h_0 to h_B) occurring at a radial distance r_B, if the ratio between r_B/h_B is less than 5. Conversely, truncations are changes in the slope (h_T) of the surface-brightness profiles happening at a radius r_T, with a ratio r_T/h_T greater than 5. Applying this recipe to the whole sample of galaxies, we can analyse both features separately and study whether they are actually different phenomena. We note that in Comerón et al. (2012) a slightly different notation is used, in which 'break' describes all changes in slope, with Type II
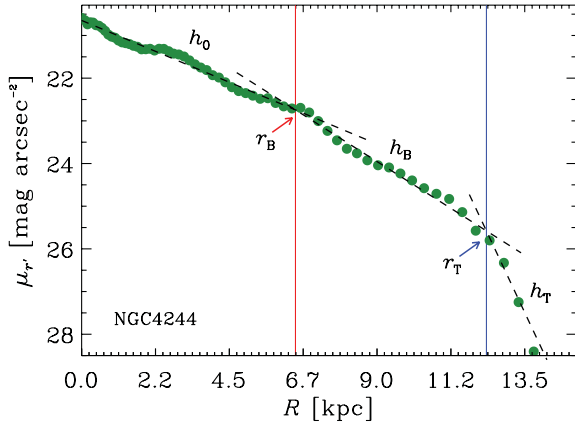
Figure 8. Exemplification of the meaning of the parameters h_0, h_B, h_T, r_B and r_T using the r'-band surface-brightness profile (NGC 4244).

breaks being termed 'truncation' and Type III breaks being called 'antitruncations'. Our galaxies have been traced out further than in most previous studies, and this leads to our recognition of a second break in some cases. Breaks with $r_B/h_B > 5$ are called 'truncation', in keeping with previous nomenclature, even if there is no clear evidence for a sharp end to the disc. In fact, most of our truncations are transitions to a far-outer region that may be as exponential as the inner regions, although with a steeper decline. Studies extending outer disc surface photometry to greater radii with star counts do not find a sudden drop-off either (Richardson et al. 2008; Saha et al. 2010; Grossi et al. 2011; Barker et al. 2012; Radburn-Smith et al. 2012).

In Fig. 10 we show three examples of a galaxy with break *and* truncation (top), a galaxy where only the break has been detected (middle) and a galaxy with just a truncation (bottom) using our criteria. The vertical lines (red and blue in the online article) mark the break and truncation radii (respectively) in both the surface-brightness profiles and in the galaxy images. It its clear from Fig. 10 that the break occurs closer to the galactic centre compared with the truncation, which appears near the very end of the optical disc. Also, the change in the exponential scalelength seems to be stronger after the truncation than after the break.

We show in Table A4 the summary of all the measurements and the derived quantities for breaks and truncations.

4.4 Inner break analysis

Looking at the relative frequencies of the different profile types around the inner break radius, 82 ± 16 per cent[3] (28 cases) of our galaxies can be classified as TII (i.e. after the break there is a downbending in their surface-brightness distribution). For the TI and TIII cases, we found frequencies of 6 ± 4 per cent (2 cases) and 12 ± 6 per cent (4 cases) respectively. These values are different from those found by Pohlen & Trujillo (2006) (10 per cent/60 per cent/ 30 per cent for TI/TII/TIII) but two factors must be taken into account. On one hand, as we have only 34 galaxies, the statistical analysis is not as robust as in the case of Pohlen & Trujillo (2006). On the other hand, the study of Pohlen & Trujillo (2006) includes morphological types from Sb to Sdm while our sample only collects

Sc or later spiral types. It is well established (Pohlen & Trujillo 2006; Gutiérrez et al. 2011) that there exists a trend in the sense that TII becomes dominant in late-type galaxies. If the statistics of Pohlen & Trujillo (2006) are recalculated for the same morphological range as used in the current paper, we find that the relative frequencies become compatible (6 ± 4 per cent versus 12 ± 7 per cent for TI, 82 ± 16 per cent versus 76 ± 17 per cent for TII and 12 ± 6 per cent versuss 12 ± 7 per cent for TIII).

The mean surface-brightness value for the TII inner breaks is 22.5 ± 0.1 mag arcsec^{-2} in the r' band. For the others bands employed in the current paper, the mean surface brightnesses at the break radius are listed in Table A5. We find a mean radius equal to 7.9 ± 0.9 kpc, which is in agreement with the result of Pohlen & Trujillo (2006), who found a typical radius of 9 ± 3 kpc. The break scalelength h_B has a mean value of 2.7 ± 0.3 kpc.

Fig. 11 shows the values for the r'-band surface brightness, the $(g' - r')$ colour and the radial distance $\{\mu_{r'}, (g' - r'), r_B\}$ measured at the break radius (only TII profiles), plotted against M_B and the maximum rotational velocity of the galaxy. In each plot the Spearman's rank correlation coefficient is overplotted.[4] Significant correlations are found between the break radius and M_B and between the $(g' - r')$ colour at the break and the maximum rotational velocity (top right and bottom left panels, respectively). This correlation between the break radius and M_B and the fact that our sample is limited to objects brighter than $M_B = -17$ can explain why we marginally measure a mean break radius smaller than Pohlen & Trujillo (2006), whose galaxies were brighter than $M_B = -18.4$.

4.5 Truncation analysis

We found that all the profiles are downbending and steeper after the truncation than after the inner break, with a mean value for the scalelength h_T equal to 1.5 ± 0.1 kpc. The r'-band surface brightness has a mean value at the truncation radius of 24.1 ± 0.2 mag arcsec^{-2} (see Table A5 for the mean values in the other bands) and the averaged radial distance is 14 ± 2 kpc. On average, the 3σ sky level in the r' band is ~ 3.5 mag arcsec^{-2} dimmer than the typical surface brightness of the truncations, so our results are not strongly affected by the sky-subtraction process. The typical signal-to-noise ratio at the truncation radius is ~ 10 in the r' band.

In the case of truncations, we also looked for correlations between the same set of parameters as in Fig. 11 but measured, obviously, at the truncation radius. The results of the analysis are in Fig. 12, where strong correlations appear between M_B and the maximum rotational velocity and the radius where the truncation occurs.

It should be noted that the statistics derived in Figs 11 and 12 are heavily influenced by a couple of points due to NGC 5907 and NGC 5529. The latter has a boxy/peanut bulge and a warped outer disc, while NGC 5907 shows a bulge and a small warp too. If we exclude those two galaxies from the statistical analysis, the Spearman's rank correlation coefficient changes from 0.50 to 0.44 in the $V_{rot}(max)$ versus r_B relation and from 0.81 to 0.73 in the $V_{rot}(max)$ versus r_T relation.

---

[3] The errors are given by $\Delta T_i = \sqrt{N_{T_i}}/N_S$, where N_{T_i} is the number of T_i profiles in a sample of N_S elements.

[4] The Spearman's rank correlation coefficient varies between -1 and 1. The closer its absolute value is to 1, the stronger the correlation.
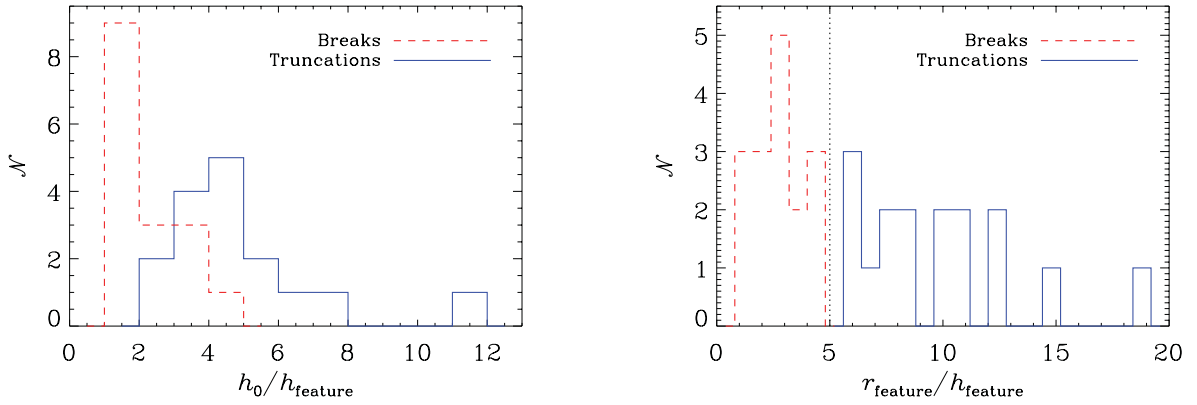
Figure 9. Histograms representing the distribution of breaks and truncation versus the h_0/h_{feature} (left) and the $r_{\text{feature}}/h_{\text{feature}}$ (right) parameters, where h_0 is the innermost exponential scalelength (between the galactic centre and the first break) and h_{feature} is the exponential scalelength after the first break (*break*) or after the second break (*truncation*), measured in the SDSS r' band. r_{feature} represents the distance from the centre of the galaxy where the break or the truncation is measured. The degeneracy shown in the left panel between both features is broken in the right panel.
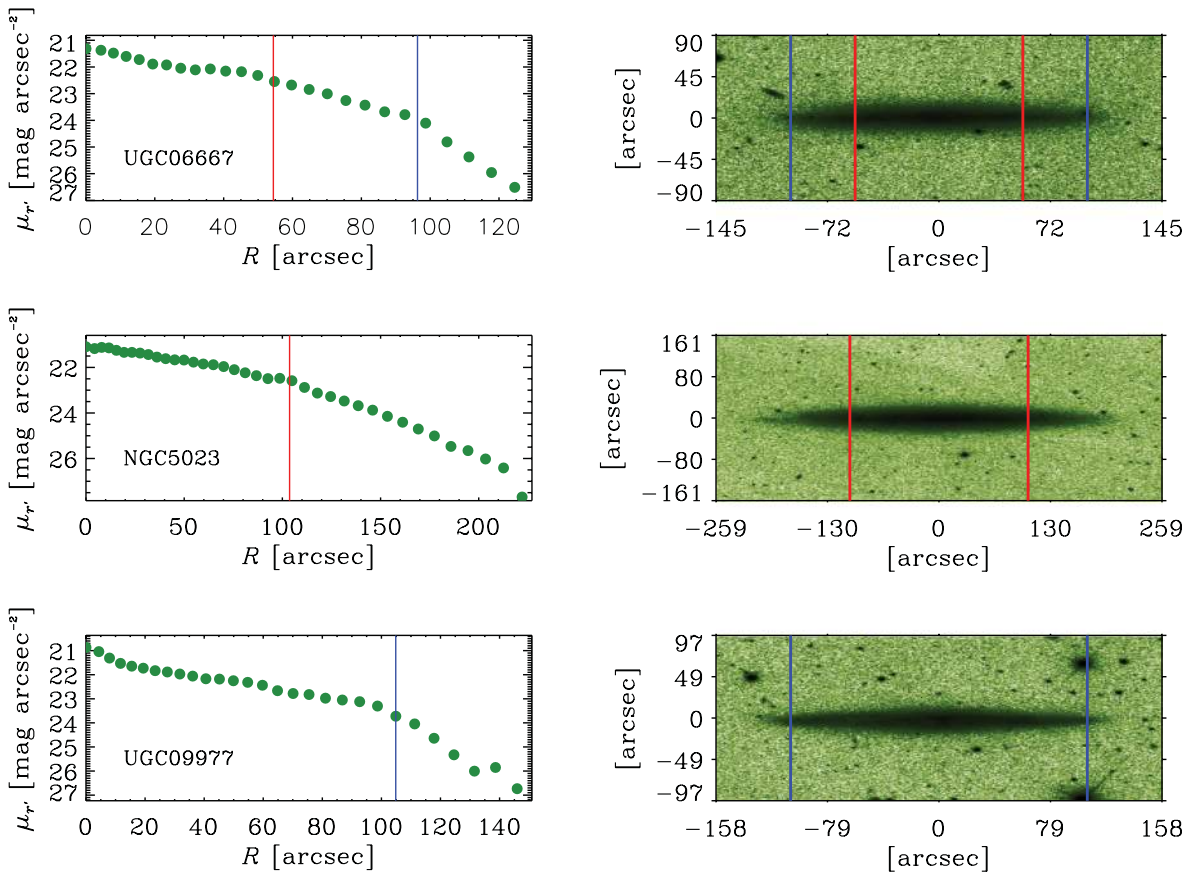
Figure 10. Upper panel: UGC 6667 showing both a break (red line in the online article) and a truncation (blue line in the online article). Middle panel: the galaxy NGC 5023, with a break marked in red in the online article. There is a hint of a truncation around $r \sim 210$ arcsec but, as there were not enough points above the surface-brightness limit, we did not perform a fit over that region. Lower panel: galaxy UGC 9977, where we only detected a truncation. The right column shows the position of the breaks and truncations over the galaxy images.

5 DISCUSSION

5.1 Comparison with previous studies

Inner breaks and truncations, as defined in Section 4.3, have different characteristic parameters. Breaks appear closer to the galactic centre compared with truncations ($r_B \sim 8$ kpc; $r_T \sim 14$ kpc) and the typical exponential scalelength is also smaller after breaks than after truncations ($h_B \sim 3$ kpc; $h_T \sim 1.5$ kpc). In addition, we have found that the ratio between the mean radius for breaks and truncations ($\langle r_T \rangle / \langle r_B \rangle = 1.8 \pm 0.5$ among our sample of galaxies) is very similar to the ratio $\langle r_{\text{EO}}/h_0 \rangle / \langle r_{\text{FO}}/h_0 \rangle = 1.8 \pm 0.9$ between the
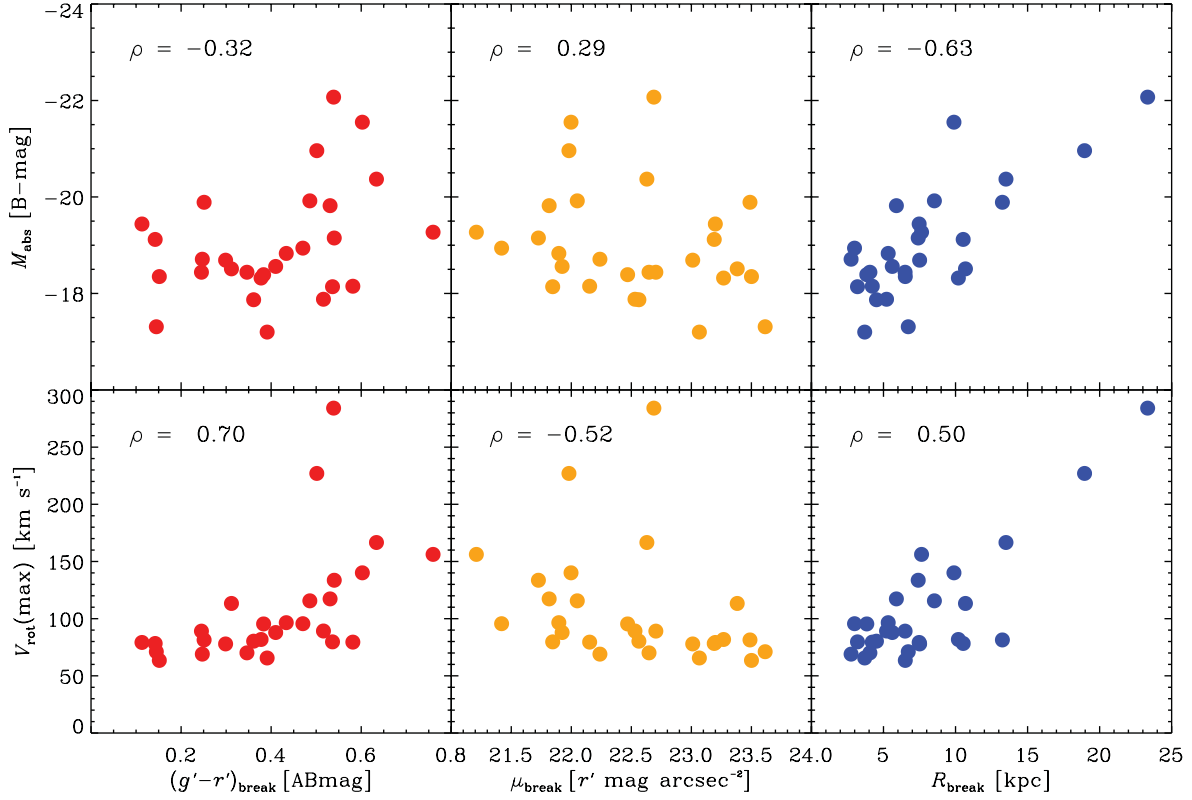
Figure 11. Breaks: correlations between $(g' - r')$ (left), $\mu_{r'}$ (centre) and r_B (right) with the *B*-band absolute magnitude M_B (top) and the maximum rotational velocity (bottom). The Spearman's rank correlation coefficient (ρ) is overplotted.
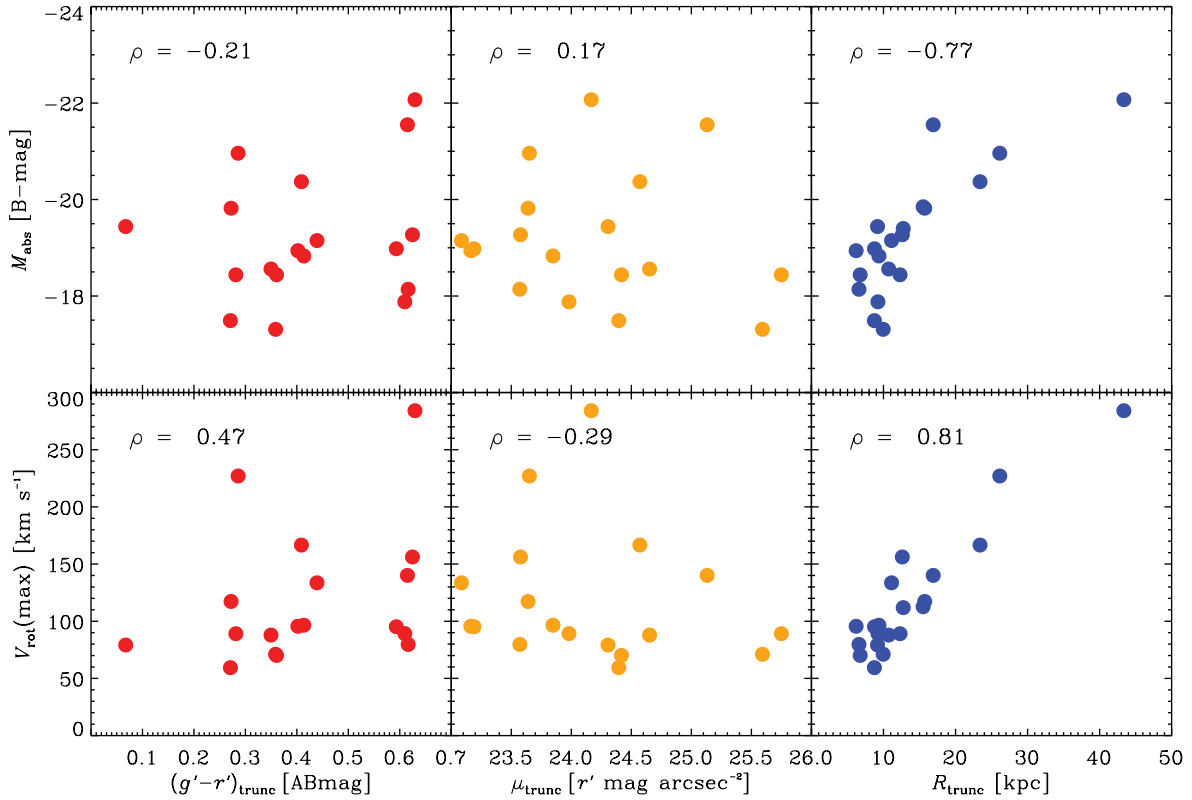

Figure 12. Truncations: correlations between $(g' - r')$ (left), $\mu_{r'}$ (centre) and r_T (right) with the *B*-band absolute magnitude M_B (top) and with the maximum rotational velocity (bottom). The Spearman's rank correlation coefficient (ρ) is overplotted.

break radii in edge-on galaxies from van der Kruit (1987) and those in face-on galaxies from Pohlen & Trujillo (2006). Since the latter results are normalized to the innermost exponential scalelength, this quotient between edge-on and face-on measurements can be only compared to our results fairly if the innermost scalelength h_0 remains unchanged while looking at a galaxy in both projections. In this sense, Pohlen et al. (2007) found that their deprojected h_0 values match with the range given by Pohlen & Trujillo (2006) if the influence of dust is taken into account.

It is possible, then, that the previous discrepancies found for the position of the breaks between edge-on and face-on studies can be explained as follows. Face-on studies usually measure the break radius but the truncation happens (due to the orientation) at very low surface brightness (typically ~ 26.5 mag arcsec^{-2}), probably beyond the surface-brightness limit. In contrast, thanks to the line-of-sight integration, in the edge-on observations the truncation appears at higher surface brightness and it can be detected. The transition to a steeper decline after the break in the edge-on profiles can be smoothed because of this particular projection too, making it more difficult to detect this feature in edge-on galaxies than in the face-on counterpart, and for this reason it may have remained unnoticed in previous papers (but see Comerón et al. 2012).

A natural prediction of our analysis is that truncations should be systematically observed in face-on projections if the images are deep enough. Just recently Bakos & Trujillo (2012) used very deep data from SDSS Stripe82 to explore the very faint regimes of discs in face-on projections by obtaining surface-brightness profiles down to ~ 30 r'-band mag arcsec^{-2}. Bakos & Trujillo have not found any clear evidence for a truncation in these profiles but they have reported that the surface-brightness profiles of stellar discs show a smooth continuation into what they have identified as stellar haloes. These stellar haloes start to dominate the surface-brightness profiles at ~ 27.5. r'-band mag arcsec^{-2} Coincidently, this means that observing truncations in face-on projections could be hindered due to a lack of contrast between disc and stellar halo components. The result of Bakos & Trujillo (2012) would, if confirmed, point out that our only opportunity of studying truncations in spiral galaxies might be limited to edge-on observations, unless an accurate parametrization and subtraction of the stellar halo component can be performed.

5.2 Break-truncation scenario

If breaks and truncations are actually two differentiated features, the two main theories (see Section 1) proposed to explain break formation are not mutually exclusive, each playing a role at different distances from the galactic centre. On the one hand, the averaged value found here for the break radius is compatible with the face-on picture of a break caused by a threshold for star formation in the disc. On the other hand, we have found a mean truncation radius that is extremely well correlated with the maximum rotational velocity of the galaxy ($\rho = 0.81$). The above ideas are reinforced if we look at the different degree of correlations between the break/truncation radius and the maximum rotational velocity.

We can calculate the specific angular momentum of the disc to exemplify the differences between the two breaks by following the empirical expression given by Navarro & Steinmetz (2000):

$$j_{\text{disc}} \approx 1.3 \times 10^3 \left[\frac{V_{\text{rot}}(\text{max})}{200 \text{ km s}^{-1}} \right]^2 \text{ km s}^{-1} \, h^{-1} \text{ kpc}.$$
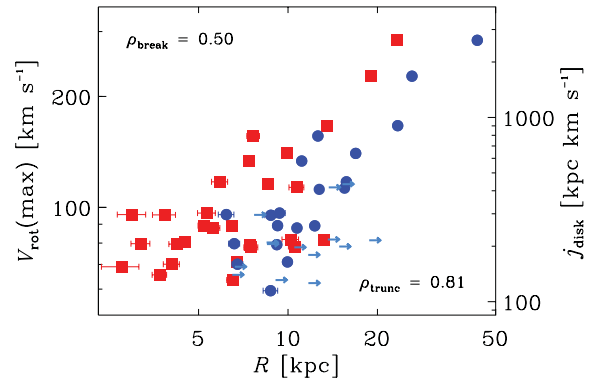
Figure 13. Correlations between the positions of the inner breaks (squares, red in the online article) and the radial position of the truncations (dots, blue in the online article) versus the maximum rotational velocity and the specific angular momentum of the disc. Arrows (light blue in the online article) represent r_{max} as defined in Section 4.1. These arrows correspond to those galaxies where no truncation has been detected (so they should be considered as a lower limit for the truncation radius). The Spearman's rank correlation coefficients for breaks (top left) and truncations (bottom right) are overplotted.

Note that, following the equation above, the derived specific angular momentum of the disc is just a rescaling of the maximum rotational velocity of the galaxy. This specific angular momentum is therefore shown as auxiliary information, but it has no influence on further results.

Fig. 13 shows how the break and truncation radii correlate with the maximum rotational velocity and with the specific angular momentum of the disc. The Spearman's rank coefficient reveals a very strong correlation ($\rho_{\text{trunc}} = 0.81$) between the maximum rotational velocity (and the specific angular momentum of the disc) and the truncation radius. In contrast, the correlations between the same dynamical parameters and the break radius are significantly weaker ($\rho_{\text{break}} = 0.50$).

From Fig. 13 it is clear that the truncation radius correlates with the maximum rotational velocity for the whole range of values in the sample, but the break radius correlates well only for those galaxies with $r_B \gtrsim 8$ kpc. Bellow this value, the break distance seems to be decoupled from the rotational velocity. In other words, for small discs with $V_{\text{rot}} < 100$ km s^{-1}, r_B and V_{rot} are not linked. The break radius seems to be strongly related to the maximum rotational velocity only when it occurs in a galaxy with significant angular momentum. This behaviour supports the picture of truncations caused by the distribution of galactic angular momentum and a break most likely related to a threshold in the gas density. Only when the rotational velocity is significant does the threshold in the star-forming gas seem to be affected by the angular momentum distribution.

In the stellar surface mass density profile, the break has almost disappeared in many cases compared with the surface-brightness profiles but the truncation barely changes (see Figs 6 and 7). In particular, we find a typical value for the ratio $\langle h_0/h_B \rangle_{\log \Sigma} = 1.6 \pm 0.1$ at the break distance. Truncations, in contrast, show a ratio $\langle h_0/h_T \rangle_{\log \Sigma} = 2.8 \pm 0.3$, associated with a quicker drop in the stellar surface mass density profile than in the break case. This is also in agreement with this *break-truncation* scenario, where a fast drop in the density of stars is expected after truncation but not necessarily after breaks, as was pointed out in Section 1.

However, two things must be noted here about the physical origin of breaks and truncations. First of all, finding a feature in a modern disc is not very clearly tied to cosmological accretion because

the disc can adjust its mass distribution during its life (e.g. Roškar et al. 2008). Thus, the origin of truncations related to the angular momentum of the protogalactic cloud should be treated carefully. Also, regarding the formation of breaks, there is observational evidence that points to some level of star formation in the outskirts of spiral galaxies (Bush et al. 2010; Barker et al. 2011), arguing against completely quenched star formation after the break radius.

Another important point regarding break-truncation differentiation is that we have measured an averaged ratio between the scale-length after breaks (h_B) and after truncations (h_T) equal to $\langle h_B/h_T \rangle = 1.9 \pm 0.4$. This means that the change in slope of the surface-brightness profile is a factor of ~ 2 stronger for truncations than for breaks. This result could explain why van der Kruit & Searle (1981), studying edge-on galaxies, found a sharp *cut-off* (truncation) in their surface-brightness profiles while face-on studies find a feature (break) that corresponds to a softer *break* in the radial light distribution (see Pohlen & Trujillo 2006, section 6 in that paper).

The fact that the ratio $r_{feature}/h_{feature}$ is a good indicator to separate breaks from truncations (see Fig. 9) can be fully understood now. For truncations, the numerator $r_{feature}$ is larger and the denominator $h_{feature}$ is smaller compared with breaks. The ratio between both quantities has, therefore, a significantly higher value for truncations than for breaks:

$$\left[\frac{r_B(\downarrow)}{h_B(\uparrow)} \right] (\Downarrow) \longleftrightarrow \left[\frac{r_T(\uparrow)}{h_T(\downarrow)} \right] (\Uparrow).$$

We can also conclude that edge-on orientation is a better tool with which to study the outermost parts of galaxies because it allows us to reach the outskirts with a higher surface brightness than in the face-on case. A disadvantage of this edge-on projection is that study of the colour and stellar surface mass density profiles is less robust than in the face-on case, due to the strong, yet measurable, influence of dust and line-of-sight integration problems (see Section 3.2). As an example, we can compare fig. 2 in the paper of Bakos et al. (2008) with Figs 11 and 12 (top left panels) in this paper. Unlike Bakos et al. (2008), we did not find any clear correlation between the $(g' - r')$ colour at the break radius and the M_B of the galaxy.

To sum up, two differentiated features can be found in the light distribution of the disc in spiral galaxies: breaks and truncations. Face-on galaxies seem to be the perfect candidates with which to study breaks because both surface-brightness profiles and colour profiles are available with moderate dust influence. The advantage of integrating along the line of sight is crucial in the case of truncations, since a truncation is a feature that happens at very low surface brightness. However, the colour profiles in the edge-on projection have to be interpreted with great care. Also, in the edge-on projection it is not possible to classify breaks depending on the morphology of the galaxy (see Pohlen & Trujillo 2006, their section 4.1) unless a two-dimensional disc decomposition is made (Gadotti 2011).

6 CONCLUSIONS

Using SDSS and S^{4}G imaging, we have found the following important aspects regarding the behaviour of surface-brightness profiles in edge-on late-type spirals.

(i) The majority of our galaxies (82 ± 16 per cent) show a TII surface-brightness profile like those found in photometric studies of face-on galaxies, with the break occurring at a mean radial distance from the galactic centre equal to 7.9 ± 0.9 kpc.

(ii) Truncations, previously described in edge-on galaxies as a quick drop in the surface-brightness profile, have been found in 20 of the 34 galaxies in our sample. This drop, also observed in the stellar surface mass density profile, occurs at an average radial distance of 14 ± 2 kpc.

(iii) For many galaxies, breaks and truncations coexist as two differentiated features in the light distribution of the discs in spiral galaxies.

(iv) Strong correlations exist between the truncation radius and the maximum rotational velocity and the specific angular momentum of the disc. These correlations are, however, less strong in the case of breaks. This result reinforces the idea that breaks are more likely a phenomenon related to a star-formation threshold whereas truncations have a strong connection with the maximum angular momentum of the galaxy.

(v) Colour and stellar surface mass density profiles are both very sensitive to the line-of-sight projection and to the presence of dust. Their interpretation in edge-on systems is not trivial and could be the cause of the differences between some of our results and those found in face-on works (e.g. correlations between M_B and break radius).

REFERENCES

Abazajian K. N. et al., 2009, ApJS, 182, 543
Azzollini R., Trujillo I., Beckman J. E., 2008, ApJ, 679, L69
Bakos J., Trujillo I., 2012, preprint (arXiv:1204.3082)

Bakos J., Trujillo I., Pohlen M., 2008, ApJ, 683, L103

Barker M. K., Ferguson A. M. N., Cole A. A., Ibata R., Irwin M., Lewis G. F., Smecker-Hane T. A., Tanvir N. R., 2011, MNRAS, 410, 504

Barker M. K., Ferguson A. M. N., Irwin M. J., Arimoto N., Jablonka P., 2012, MNRAS, 419, 1489

Barteldrees A., Dettmar R.-J., 1994, A&AS, 103, 475

Bell E. F., McIntosh D. H., Katz N., Weinberg M. D., 2003, ApJS, 149, 289

Bertin E., Arnouts S., 1996, A&AS, 117, 393

Bertin E., Mellier Y., Radovich M., Missonnier G., Didelon P., Morin B., 2002, in Bohlender D. A., Durand D., Handley T. H., eds, ASP Conf. Ser. Vol. 281, Astronomical Data Analysis Software and Systems XI. Astron. Soc. Pac., San Francisco, p. 228

Bland-Hawthorn J., Vlajić M., Freeman K. C., Draine B. T., 2005, ApJ, 629, 239

Bush S. J., Cox T. J., Hayward C. C., Thilker D., Hernquist L., Besla G., 2010, ApJ, 713, 780

Comerón S. et al., 2011, ApJ, 729, 18

Comerón S. et al., 2012, ApJ, submitted (arXiv:1209.1513)

de Grijs R., Kregel M., Wesson K. H., 2001, MNRAS, 324, 1074

de Jong R. S. et al., 2007, ApJ, 667, L49

de Vaucouleurs G., 1958, ApJ, 128, 465

Debattista V. P., Mayer L., Carollo C. M., Moore B., Wadsley J., Quinn T., 2006, ApJ, 645, 209

Elmegreen B. G., Hunter D. A., 2006, ApJ, 636, 712

Elmegreen B. G., Parravano A., 1994, ApJ, 435, L121

Erwin P., Beckman J. E., Pohlen M., 2005, ApJ, 626, L81

Erwin P., Pohlen M., Beckman J. E., 2008, AJ, 135, 20

Fall S. M., Efstathiou G., 1980, MNRAS, 193, 189

Fazio G. G. et al., 2004, ApJS, 154, 10

Ferguson A., Irwin M., Chapman S., Ibata R., Lewis G., Tanvir N., 2007, in de Jong R. S., ed., Island Universes – Structure and Evolution of Disk Galaxies. Springer, Berlin, p. 239

Freeman K. C., 1970, ApJ, 160, 811

Fry A. M., Morrison H. L., Harding P., Boroson T. A., 1999, AJ, 118, 1209

Gadotti D. A., 2011, preprint (arXiv:1101.2714)

Governato F., Willman B., Mayer L., Brooks A., Stinson G., Valenzuela O., Wadsley J., Quinn T., 2007, MNRAS, 374, 1479

Grossi M., Hwang N., Corbelli E., Grovanardi C., Okamoto S., Arimoto N., 2011, A&A, 533, A91

Gutiérrez L., Erwin P., Aladro R., Beckman J. E., 2011, AJ, 142, 145

Helou G., Madore B. F., Schmitz M., Bicay M. D., Wu X., Bennett J., 1991, in Albrecht M. A., Egret D., eds, Astrophysics and Space Science Library Vol. 171, Databases and On-line Data in Astronomy. Kluwer, Dordrecht, p. 89

Holwerda B. W. et al., 2012, A&A, 541, L5

Kennicutt R. C., Jr, 1989, ApJ, 344, 685

Kregel M., van der Kruit P. C., de Grijs R., 2002, MNRAS, 334, 646

Martínez-Serrano F. J., Serna A., Doménech-Moral M., Domínguez-Tenreiro R., 2009, ApJ, 705, L133

Navarro J. F., Steinmetz M., 2000, ApJ, 538, 477

Patterson F. S., 1940, Harvard College Observatory Bulletin, 914, 9

Paturel G., Petit C., Prugniel P., Theureau G., Rousseau J., Brouty M., Dubois P., Cambrésy L., 2003, A&A, 412, 45

Pérez I., 2004, A&A, 427, L17

Pohlen M., Trujillo I., 2006, A&A, 454, 759

Pohlen M., Balcells M., Lütticke R., Dettmar R.-J., 2004, A&A, 422, 465

Pohlen M., Zaroubi S., Peletier R. F., Dettmar R.-J., 2007, MNRAS, 378, 594

Radburn-Smith D. J. et al., 2012, ApJ, 753, 138

Richardson J. C. et al., 2008, AJ, 135, 1998

Roškar R., Debattista V. P., Stinson G. S., Quinn T. R., Kaufmann T., Wadsley J., 2008, ApJ, 675, L65

Saha A. et al., 2010, AJ, 140, 1719

Sánchez-Blázquez P., Courty S., Gibson B. K., Brook C. B., 2009, MNRAS, 398, 591

Schaye J., 2004, ApJ, 609, 667

Sheth K. et al., 2010, PASP, 122, 1397

Trujillo I., Pohlen M., 2005, ApJ, 630, L17

van der Kruit P. C., 1987, A&A, 173, 59

van der Kruit P. C., 1988, A&A, 192, 117

van der Kruit P. C., 2007, A&A, 466, 883

van der Kruit P. C., Freeman K. C., 2011, ARA&A, 49, 301

van der Kruit P. C., Searle L., 1981, A&A, 95, 105

van der Kruit P. C., Searle L., 1982, A&A, 110, 61

Vlajić M., Bland-Hawthorn J., Freeman K. C., 2009, ApJ, 697, 361

Vlajić M., Bland-Hawthorn J., Freeman K. C., 2011, ApJ, 732, 7

APPENDIX A: TABLES

Table A1. Fundamental parameters of the final sample. The distances were collected from the NED data base, while the *B*-band absolute magnitude (corrected from extinction), morphological type, morphological code (T-type) and maximum rotational velocity were obtained from the HyperLeda data base.

Galaxy	M_{abs} (*B*-mag)	Morph. type	Morph. code	Distance (Mpc)	V_{rot}(max) (km s^{-1})
IC 1197	−18.56	Sc	6.0	25.7	87.9
IC 2233	−19.44	SBc	6.4	13.4	79.2
NGC 3279	−19.27	Sc	6.5	32.5	156.2
NGC 3501	−19.15	Sc	5.9	22.9	133.6
NGC 3592	−18.14	Sc	5.3	22.7	79.7
NGC 4244	−18.44	Sc	6.1	4.6	89.1
NGC 4330	−19.92	Sc	6.3	19.5	115.6
NGC 4437	−21.55	Sc	6.0	9.8	140.1
NGC 5023	−17.87	Sc	6.0	9.0	80.3
NGC 5529	−22.07	Sc	5.3	49.5	284.1
NGC 5907	−20.96	Sc	5.4	16.3	227.0
PGC 029466	−18.71	Sc	6.2	44.8	69.0
UGC 01839	−17.20	Scd	7.1	19.1	65.6
UGC 01970	−18.98	Sc	5.9	33.9	95.2
UGC 04725	−17.49	Sc	6.1	45.4	59.4
UGC 04970	−18.51	Sc	5.7	56.7	113.3
UGC 05347	−18.94	Scd	6.5	36.0	95.6
UGC 06080	−18.69	Sc	6.5	36.3	77.9
UGC 06509	−19.12	Scd	6.6	43.8	78.3
UGC 06667	−17.88	Sc	5.9	19.8	89.2
UGC 06791	−18.83	Sc	6.5	35.7	96.5
UGC 06862	−18.32	Scd	6.7	62.2	81.8
UGC 07153	−19.40	Sc	5.9	48.0	111.9
UGC 07802	−18.44	Sc	6.1	23.2	70.1
UGC 07991	−18.15	Scd	6.6	23.2	79.5
UGC 08146	−17.31	Sc	6.4	18.2	71.1
UGC 08166	−18.78	Sc	6.0	53.4	74.3
UGC 09242	−19.89	Scd	6.6	24.0	81.4
UGC 09249	−18.35	Scd	7.2	24.8	63.5
UGC 09345	−18.39	Sc	6.4	36.6	95.4
UGC 09760	−18.72	Scd	6.6	29.8	62.3
UGC 09977	−19.85	Sc	5.3	30.5	112.7
UGC 10288	−20.37	Sc	5.3	31.7	166.6
UGC 12281	−19.82	Sd	7.5	33.9	117.3

Table A2. Position angles (in degrees) calculated in this paper and from HyperLeda for our sample of galaxies. The PA is measured from the north to the east (between $0°$ and $180°$). The mean difference between our measurements and those from HyperLeda is $0°.7$.

Galaxy	PA (HyperLeda)	PA (This paper)	Galaxy	PA (HyperLeda)	PA (This paper)
IC 1197	56.6	56.3	UGC 06080	129.4	127.2
IC 2233	172.3	171.5	UGC 06509	79.0	78.9
NGC 3279	152.0	152.0	UGC 06667	87.2	87.2
NGC 3501	28.0	27.1	UGC 06791	0.5	0.8
NGC 3592	117.7	116.5	UGC 06862	103.7	103.5
NGC 4244	42.2	47.2	UGC 07153	165.8	166.3
NGC 4330	60.0	57.9	UGC 07802	56.4	56.1
NGC 4437	85.7	82.3	UGC 07991	172.6	170.5
NGC 5023	28.3	27.8	UGC 08146	30.6	30.5
NGC 5529	114.3	113.4	UGC 08166	156.5	156.3
NGC 5907	155.5	154.5	UGC 09242	70.8	71.1
PGC 029466	179.9	180.0	UGC 09249	85.5	185.5
UGC 01839	43.5	45.8	UGC 09345	141.7	140.4
UGC 01970	22.7	22.6	UGC 09760	61.2	55.0
UGC 04725	66.2	67.3	UGC 09977	80.4	77.4
UGC 04970	104.6	104.8	UGC 10288	90.2	90.0
UGC 05347	17.0	18.2	UGC 12281	30.3	29.7

Table A3. Boundaries enclosing the different regions in each galaxy. The $[r_1, r_2]$ interval marks the limits between the galactic centre and the break, $[r_3, r_4]$ the limits between the break and the truncation and $[r_5, r_6]$ between the truncation and the end of the brightness profile.

Galaxy	r_1 (arcsec)	r_2 (arcsec)	r_3 (arcsec)	r_4 (arcsec)	r_5 (arcsec)	r_6 (arcsec)
IC 1197	0.0	40.6	49.9	86.8	86.8	98.7
IC 2233	0.0	111.3	111.3	138.6	145.9	169.2
NGC 3279	11.7	45.2	49.9	86.8	86.8	104.9
NGC 3501	11.7	64.8	64.8	104.9	104.9	131.5
NGC 3592	0.0	40.6	31.8	64.8	64.8	81.1
NGC 4244	0.0	296.3	308.1	552.4	552.4	612.2
NGC 4330	0.0	98.7	92.6	161.2	–	–
NGC 4437	0.0	203.5	212.6	372.8	372.8	416.3
NGC 5023	0.0	111.3	111.3	212.6	–	–
NGC 5529	8.0	98.7	92.6	177.4	177.4	194.5
NGC 5907	19.4	222.1	222.1	320.3	320.3	401.4
PGC 029466	0.0	15.5	19.4	36.1	–	–
UGC 01839	4.4	45.2	40.6	64.8	–	–
UGC 01970	4.4	27.5	27.5	49.9	54.7	70.1
UGC 04725	0.0	19.4	19.4	36.1	40.6	49.9
UGC 04970	0.0	40.6	40.6	54.7	–	–
UGC 05347	0.0	23.4	19.4	36.1	40.6	54.7
UGC 06080	0.0	40.6	45.2	59.7	–	–
UGC 06509	0.0	49.9	49.9	75.5	–	–
UGC 06667	0.0	45.2	45.2	92.6	98.7	131.5
UGC 06791	0.0	31.8	40.6	54.7	54.7	64.8
UGC 06862	4.4	31.8	36.1	49.9	–	–
UGC 07153	0.0	49.9	–	–	54.7	70.1
UGC 07802	4.4	40.6	40.6	59.7	59.7	75.5
UGC 07991	4.4	31.8	40.6	75.5	–	–
UGC 08146	0.0	70.1	75.5	111.3	111.3	124.6
UGC 08166	0.0	27.5	27.5	40.6	–	–
UGC 09242	0.0	104.9	124.6	177.4	–	–
UGC 09249	4.4	49.9	54.7	75.5	–	–
UGC 09345	8.0	27.5	31.8	49.9	–	–
UGC 09760	0.0	49.9	64.8	81.2	–	–
UGC 09977	11.7	98.7	–	–	111.3	131.5
UGC 10288	11.7	92.6	98.7	138.6	153.5	169.2
UGC 12281	0.0	40.6	40.6	98.7	98.7	111.3

Table A4. Types of profiles and measured quantities at the break distance (B subscript) and at the truncation radius (T subscript). Here, *nd* represents a non-detected truncation. The typical error for the $(g' - r')$ colour profile is 0.10 AB mag at the break radius and 0.22 AB mag at the truncation radius.

Galaxy	Type	r_B		r_T		μ_B	μ_T	$(g' - r')_B$	$(g' - r')_T$
		(kpc)	(arcsec)	(kpc)	(arcsec)	$\left(\frac{r'\text{mag}}{\text{arcsec}^2}\right)$	$\left(\frac{r'\text{mag}}{\text{arcsec}^2}\right)$	(AB mag)	(AB mag)
IC 1197	II	5.6	45.0	10.7	86.0	21.9	24.7	0.41	0.35
IC 2233	II	7.48	115.5	9.17	141.7	23.20	24.31	0.11	0.07
NGC 3279	II	7.64	48.4	12.61	80.0	21.21	23.58	0.76	0.62
NGC 3501	II	7.41	66.8	11.12	100.2	21.73	23.09	0.54	0.44
NGC 3592	II	3.19	29.0	6.59	59.8	21.84	23.57	0.54	0.62
NGC 4244	II	6.50	289.5	12.30	548.1	22.70	25.75	0.25	0.28
NGC 4330	II	8.53	90.2	*nd*	*nd*	22.05	*nd*	0.49	1.32
NGC 4437	II	9.89	209.0	16.90	357.2	22.00	25.13	0.60	0.61
NGC 5023	II	4.51	103.7	*nd*	*nd*	22.56	*nd*	0.36	0.49
NGC 5529	II	23.33	97.2	43.37	180.6	22.69	24.17	0.54	0.63
NGC 5907	II	18.95	237.2	26.14	327.2	21.98	23.65	0.50	0.29
PGC 029466	II	2.75	13.2	*nd*	*nd*	22.24	*nd*	0.25	0.52
UGC 01839	II	3.70	39.9	*nd*	*nd*	23.07	*nd*	0.39	0.23
UGC 01970	III	3.89	23.7	8.75	53.3	21.94	23.19	0.74	0.59
UGC 04725	III	4.23	19.2	8.74	39.7	23.13	24.40	0.31	0.27
UGC 04970	II	10.69	38.9	*nd*	*nd*	23.38	*nd*	0.31	0.92
UGC 05347	II	2.99	17.9	6.20	37.1	21.42	23.16	0.47	0.40
UGC 06080	II	7.51	42.7	*nd*	*nd*	23.01	*nd*	0.30	0.38
UGC 06509	II	10.53	49.7	*nd*	*nd*	23.19	*nd*	0.14	0.32
UGC 06667	II	5.21	54.4	9.22	96.3	22.53	23.98	0.52	0.61
UGC 06791	II	5.33	30.8	9.37	54.1	21.90	23.85	0.43	0.41
UGC 06862	II	10.20	33.8	*nd*	*nd*	23.27	*nd*	0.38	0.71
UGC 07153	I	–	–	12.74	54.8	–	23.49	0.84	0.23
UGC 07802	II	4.06	36.1	6.76	60.2	22.65	24.42	0.35	0.36
UGC 07991	II	4.22	37.5	*nd*	*nd*	22.15	*nd*	0.58	0.43
UGC 08146	II	6.72	76.1	9.96	112.7	23.61	25.59	0.14	0.36
UGC 08166	III	6.85	26.4	*nd*	*nd*	23.89	*nd*	0.25	0.14
UGC 09242	II	13.25	113.9	*nd*	*nd*	23.49	*nd*	0.25	0.54
UGC 09249	II	6.51	54.2	*nd*	*nd*	23.50	*nd*	0.15	0.15
UGC 09345	II	3.84	22.6	*nd*	*nd*	22.47	*nd*	0.38	0.40
UGC 09760	III	8.26	57.2	*nd*	*nd*	23.77	*nd*	0.25	0.28
UGC 09977	I	–	–	15.50	104.8	–	23.28	1.57	0.43
UGC 10288	II	13.50	87.7	23.40	152.1	22.63	24.57	0.63	0.41
UGC 12281	II	5.89	35.9	15.72	95.8	21.82	23.64	0.53	0.27

Table A5. Mean surface brightness at the break (second column) and truncation (fourth column) radius in the six photometric bands employed in this paper.

Band	Break $\left(\frac{\text{mag}}{\text{arcsec}^2}\right)$	$\pm\Delta$ $\left(\frac{\text{mag}}{\text{arcsec}^2}\right)$	Truncation $\left(\frac{\text{mag}}{\text{arcsec}^2}\right)$	$\pm\Delta$ $\left(\frac{\text{mag}}{\text{arcsec}^2}\right)$
u'	24.0	0.1	25.7	0.2
g'	22.9	0.1	24.6	0.2
r'	22.5	0.1	24.2	0.2
i'	22.3	0.2	23.9	0.2
z'	22.1	0.2	23.7	0.2
3.6 μm	22.7	0.2	24.5	0.2

APPENDIX B: THE SAMPLE

The profiles extracted in this work. The information about how the results are presented in the following atlas is detailed in Section 3.5.
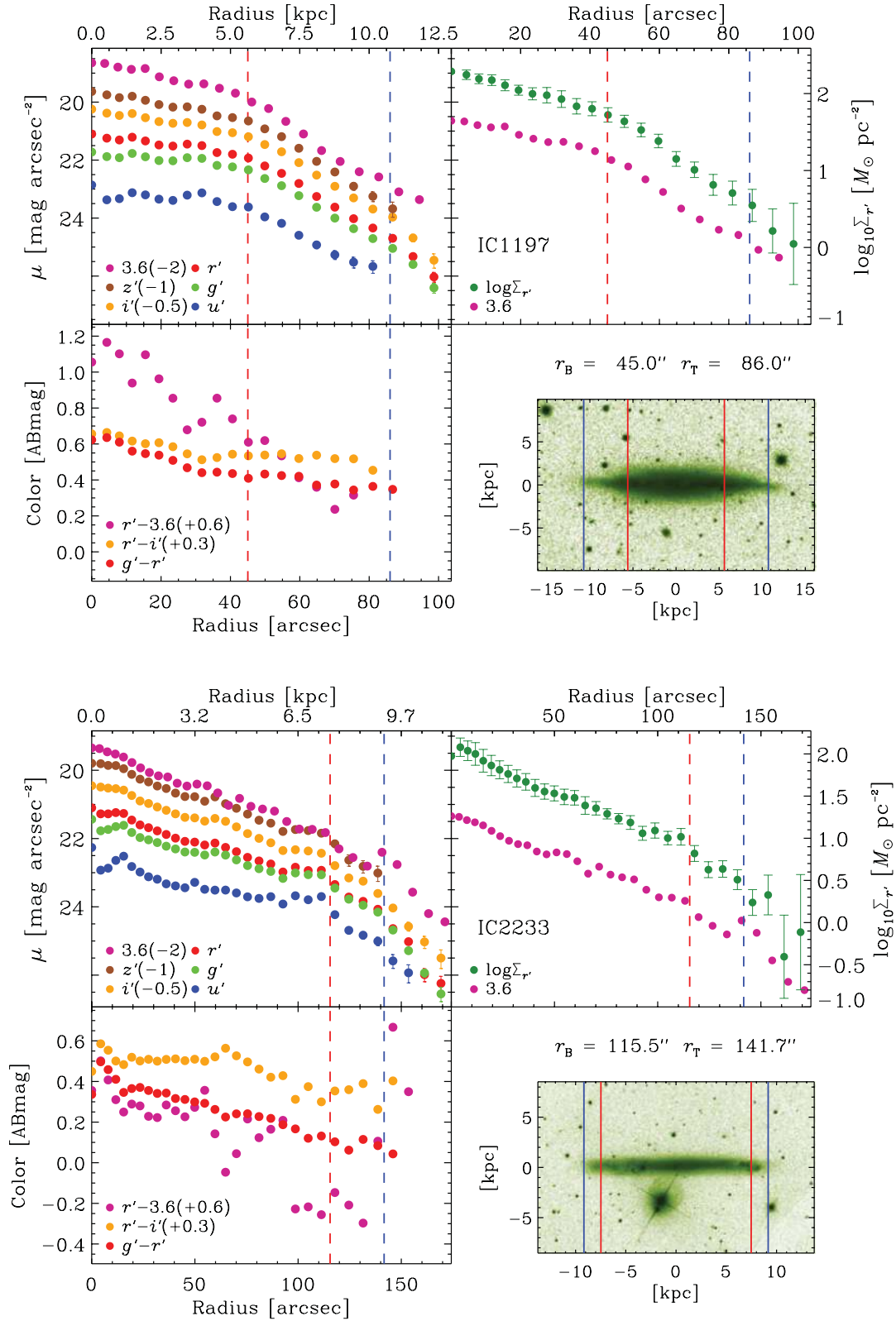
Figure B1. Surface brightness, colour and stellar surface mass density profiles. The upper left panel shows six surface brightness profiles from the different photometric bands used in the current paper. Dashed vertical lines mark where a change in the exponential behaviour happens. On the upper right panel are simultaneously plotted the stellar surface mass density profile and the 3.6 μm surface brightness profile. The bottom left panel shows the three deeper colour profiles from the available photometric bands. Lastly, the bottom right panel is occupied by a *g'*-band image of the galaxy.
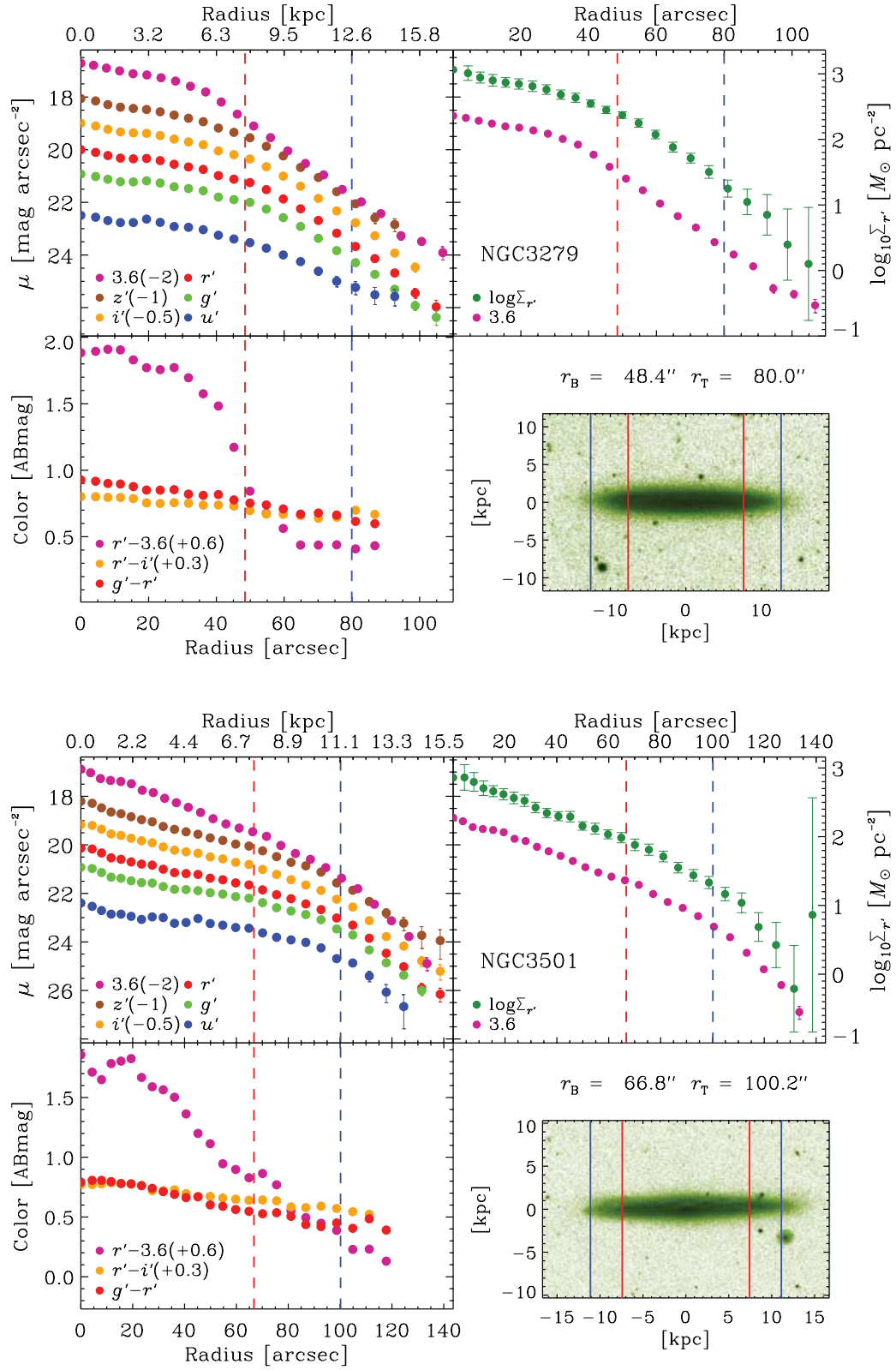
Figure B1 – *continued*
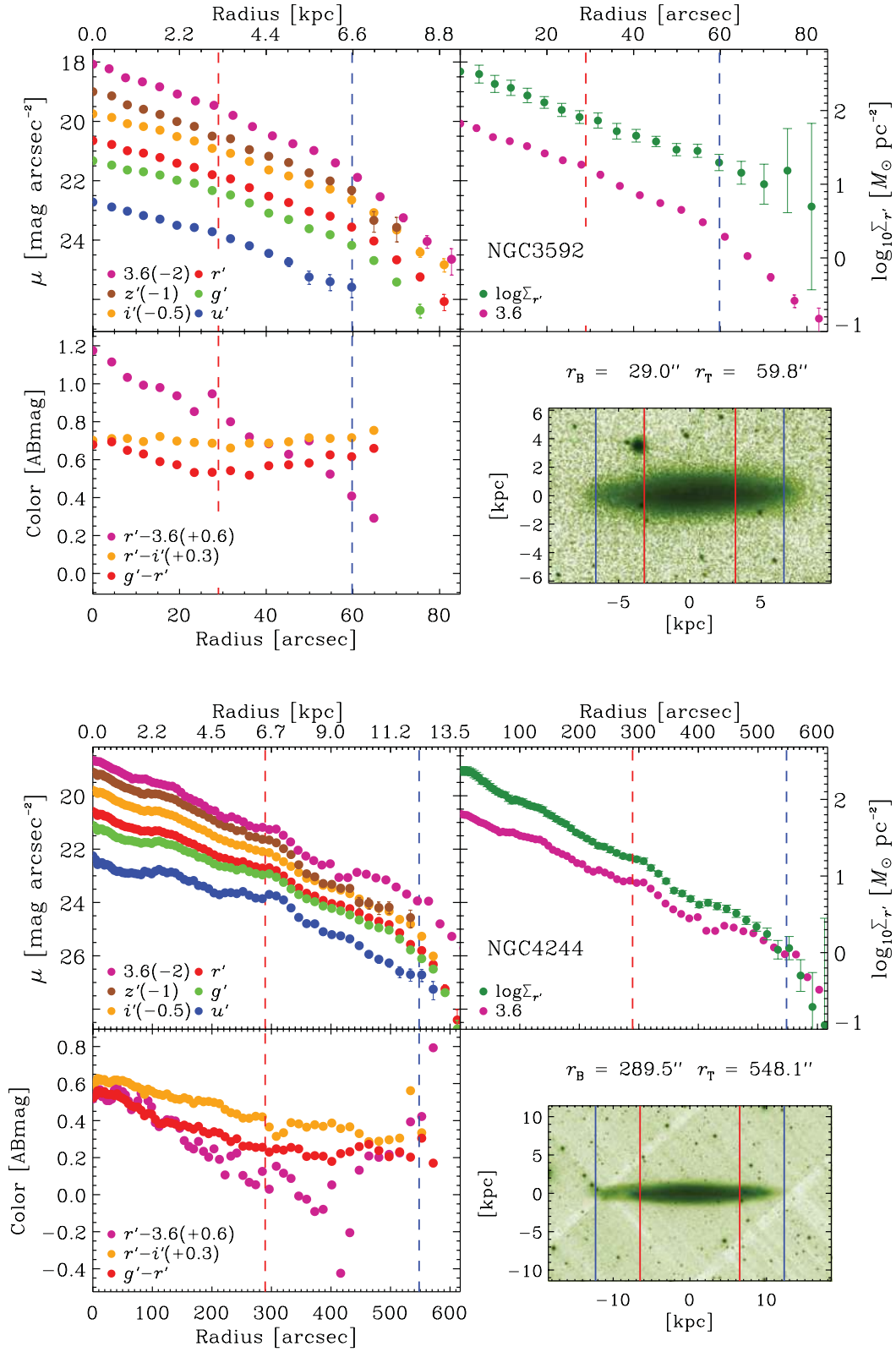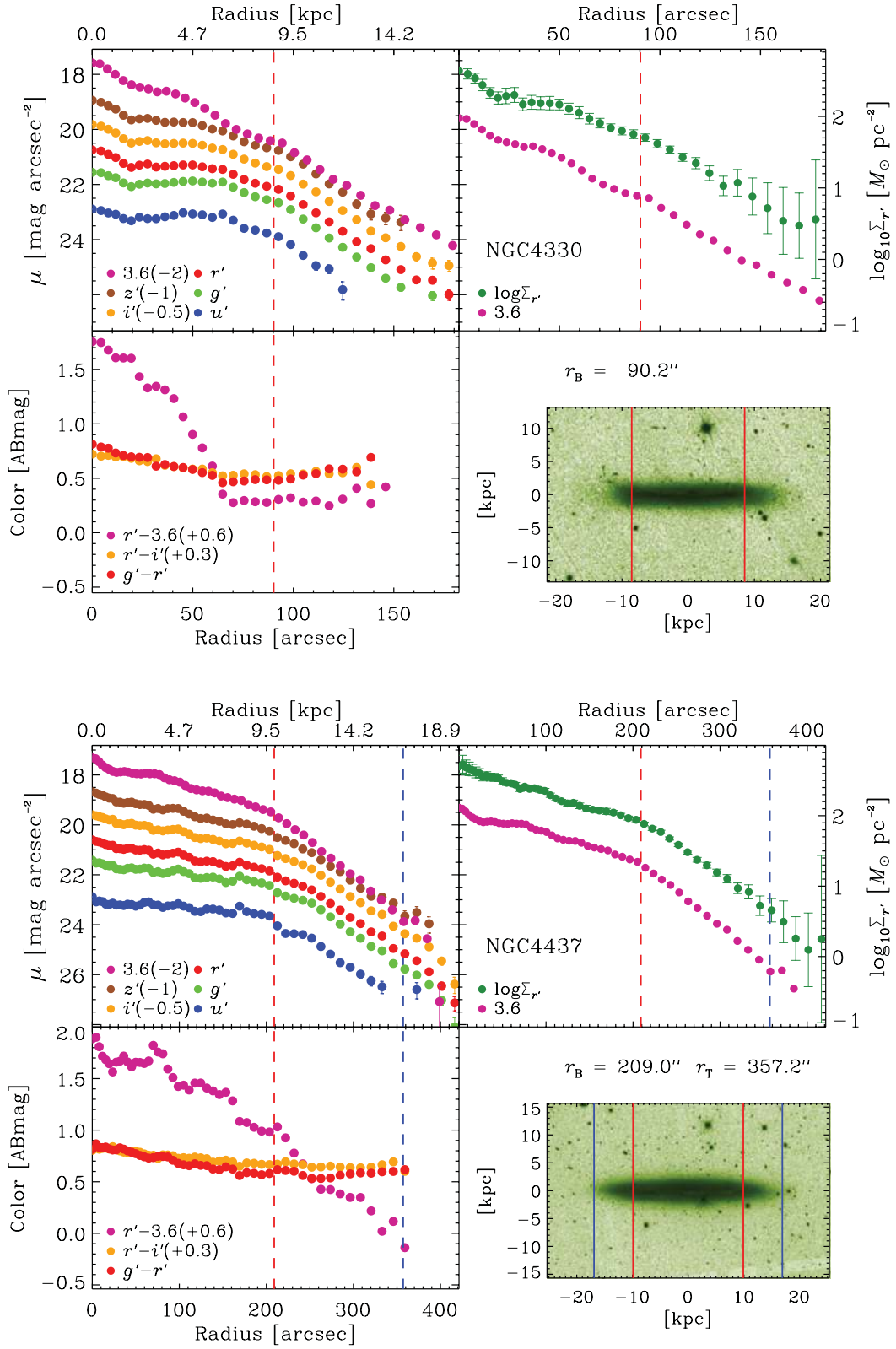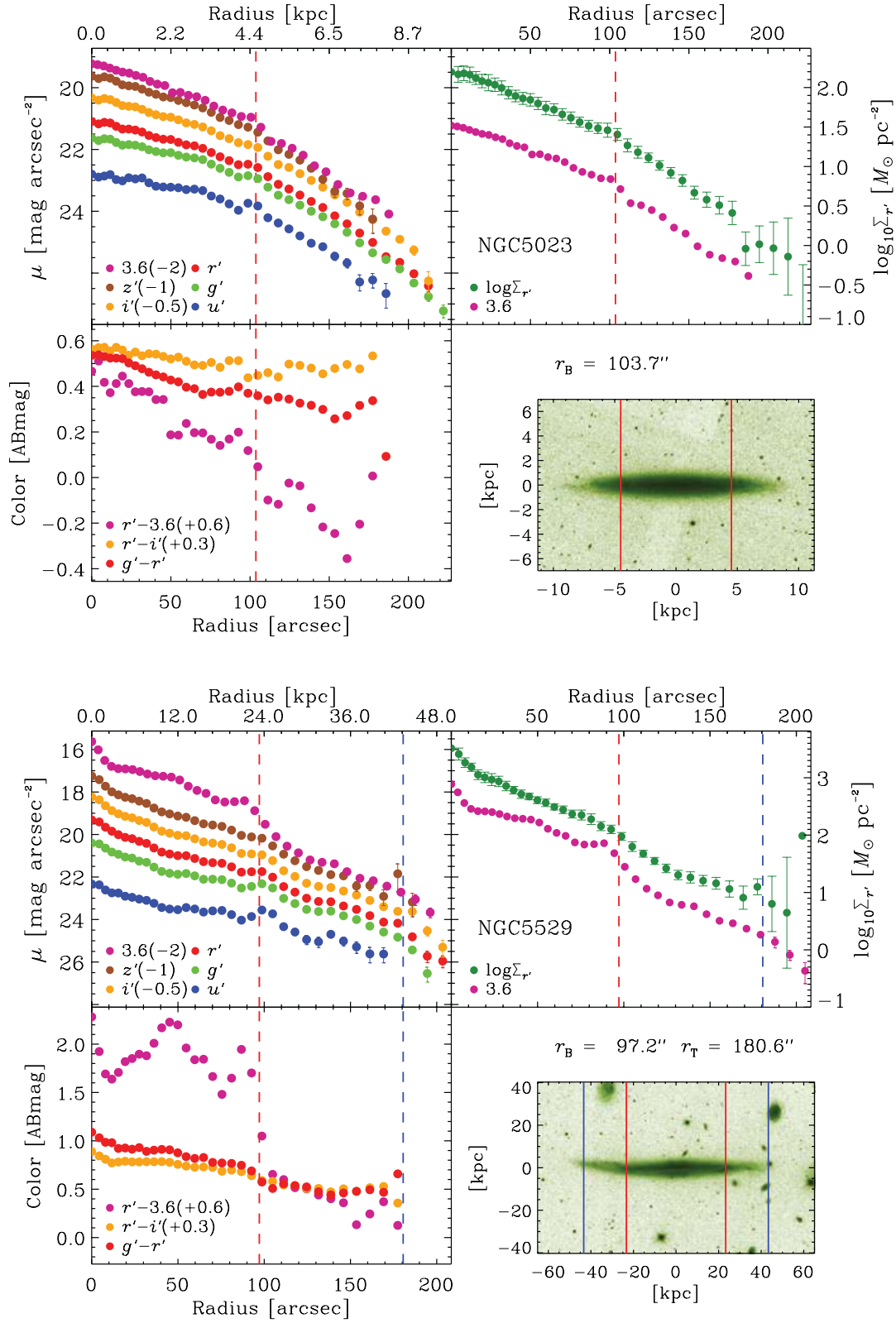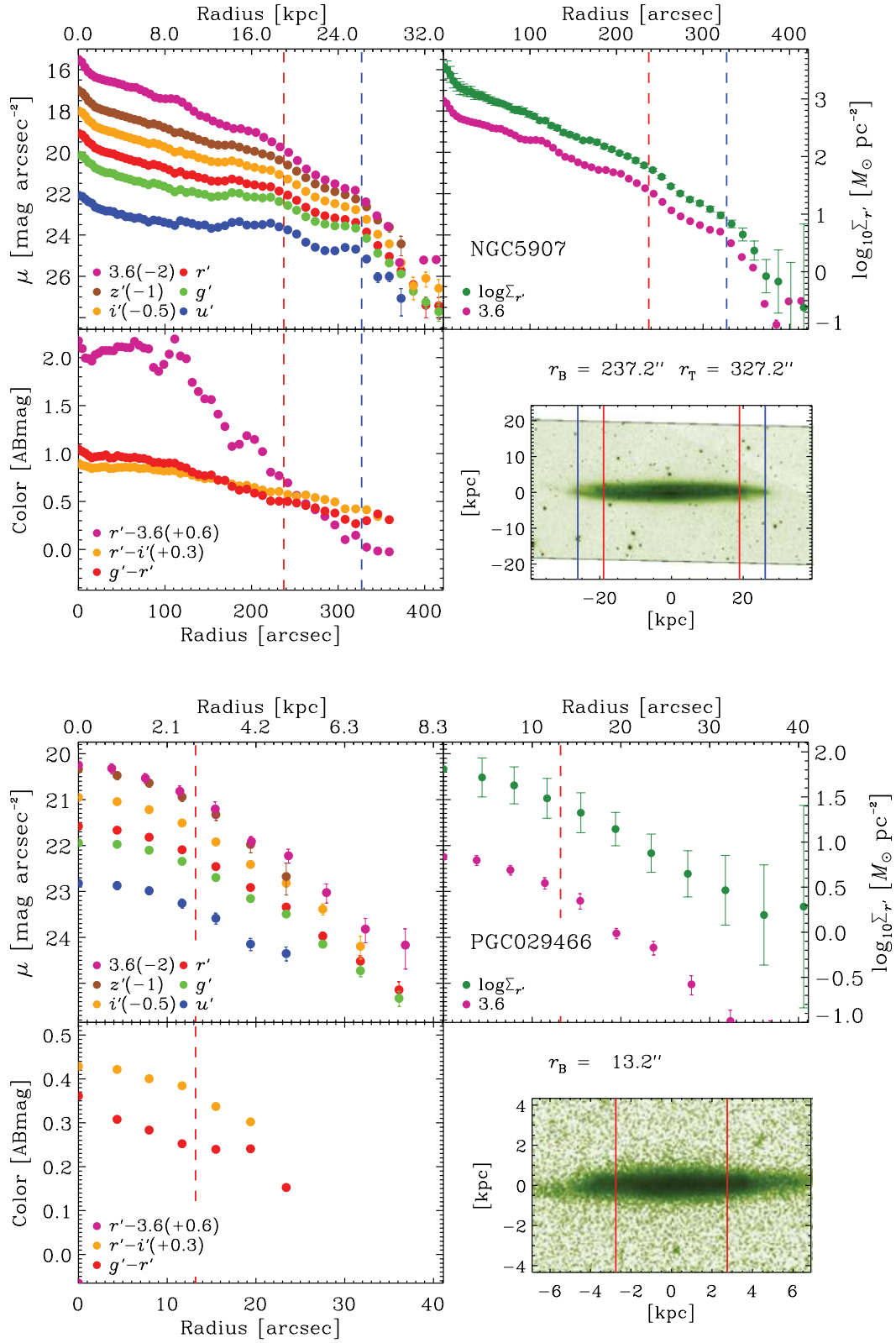
Figure B1 – *continued*
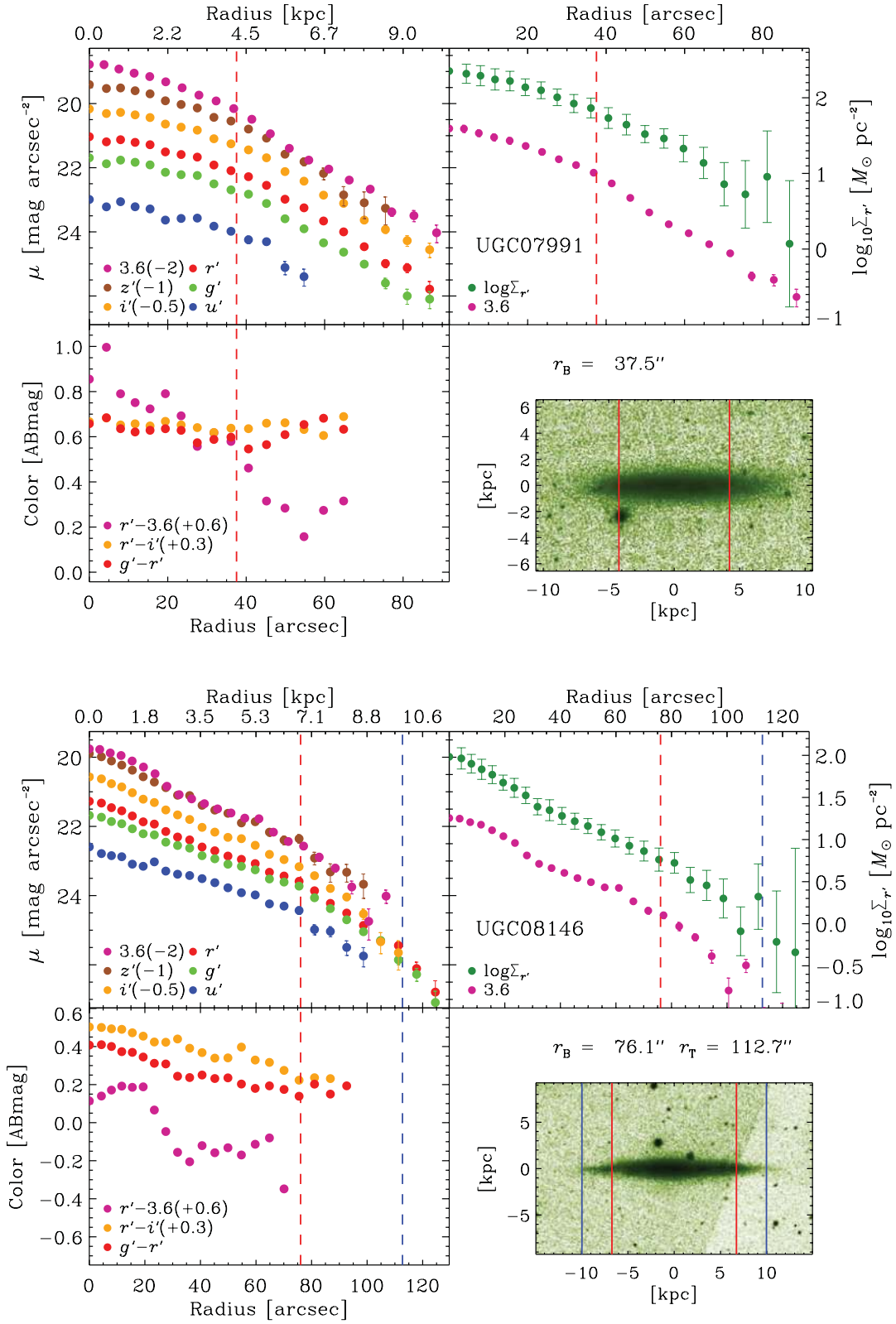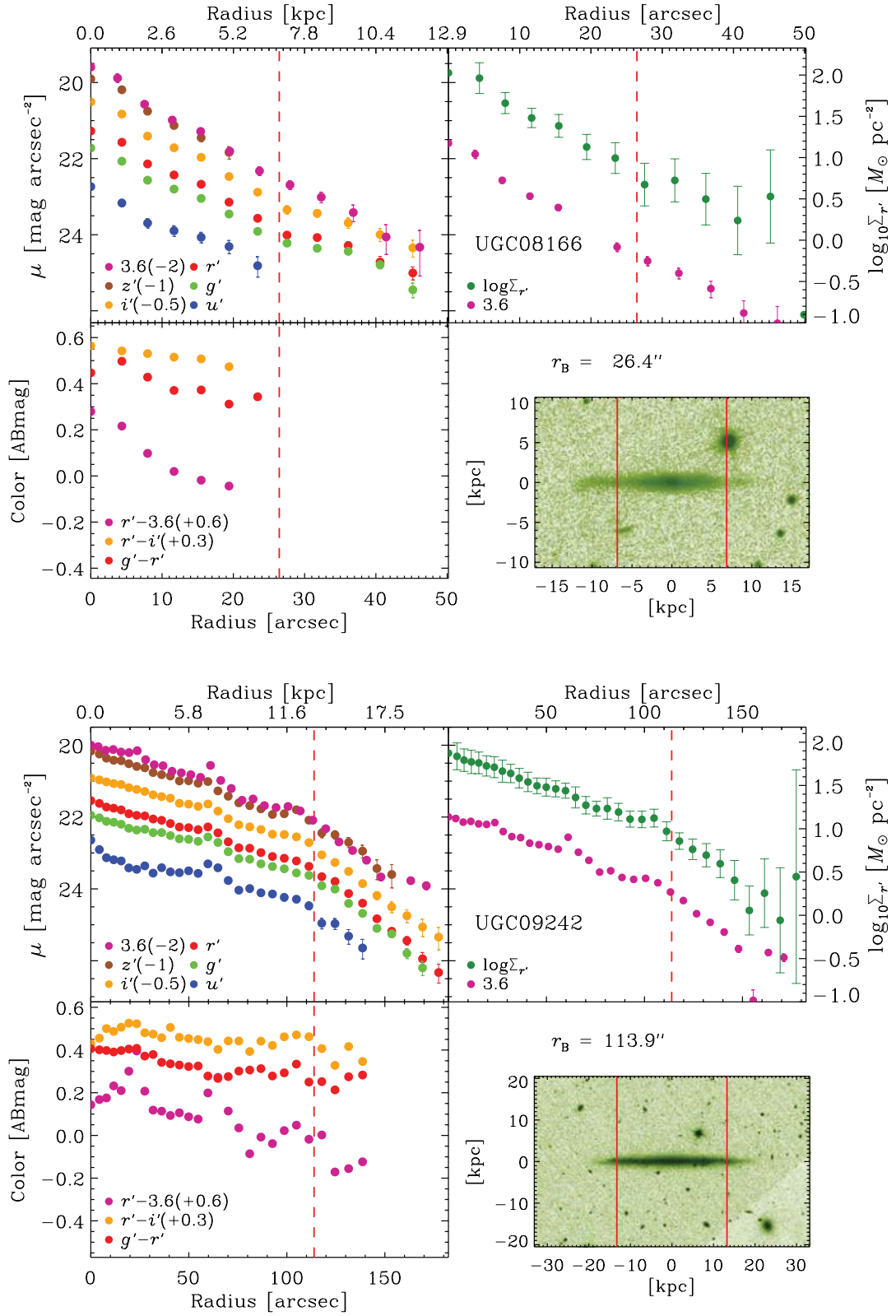
Figure B1 – *continued*

Figure B1 – *continued*

Figure B1 – *continued*
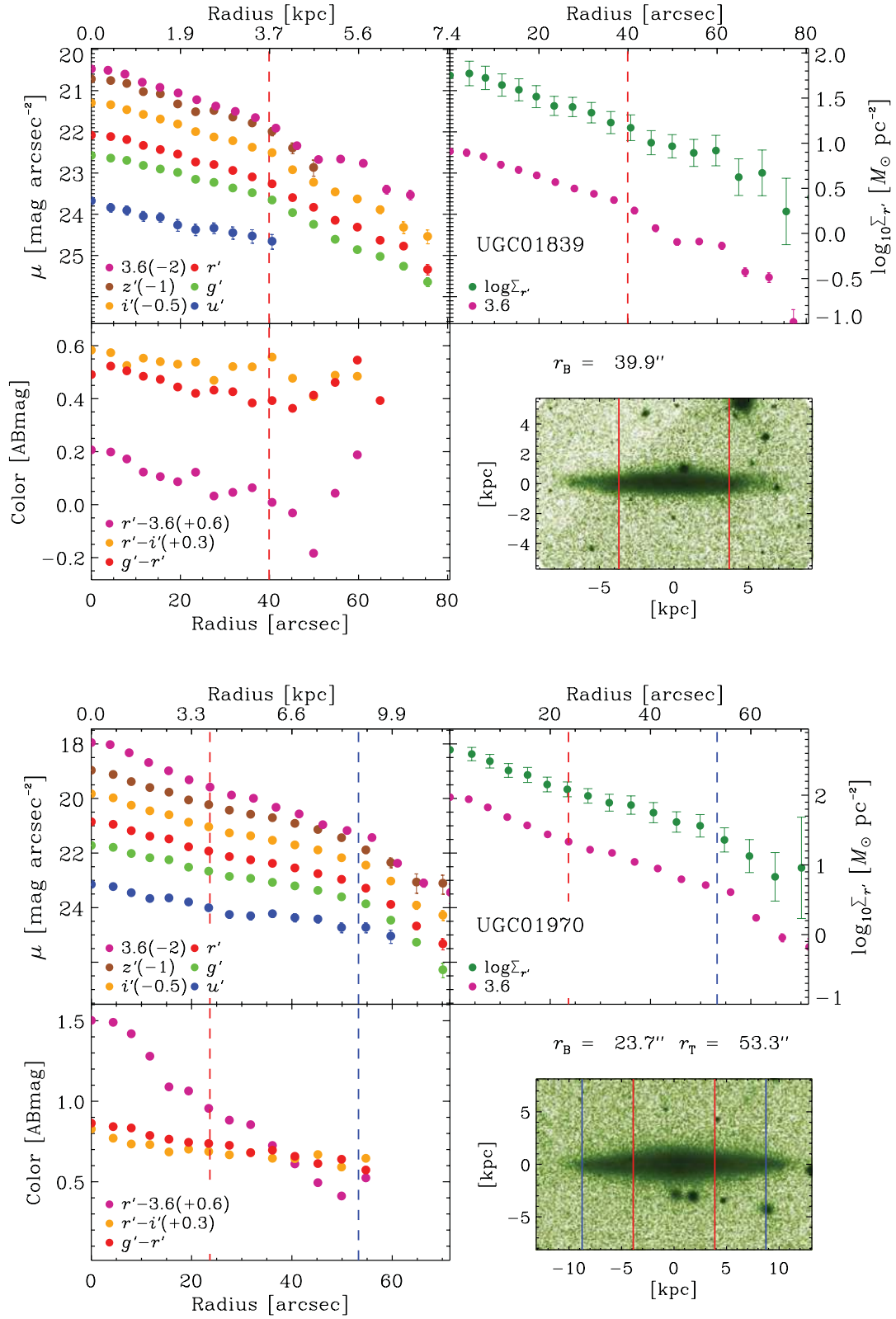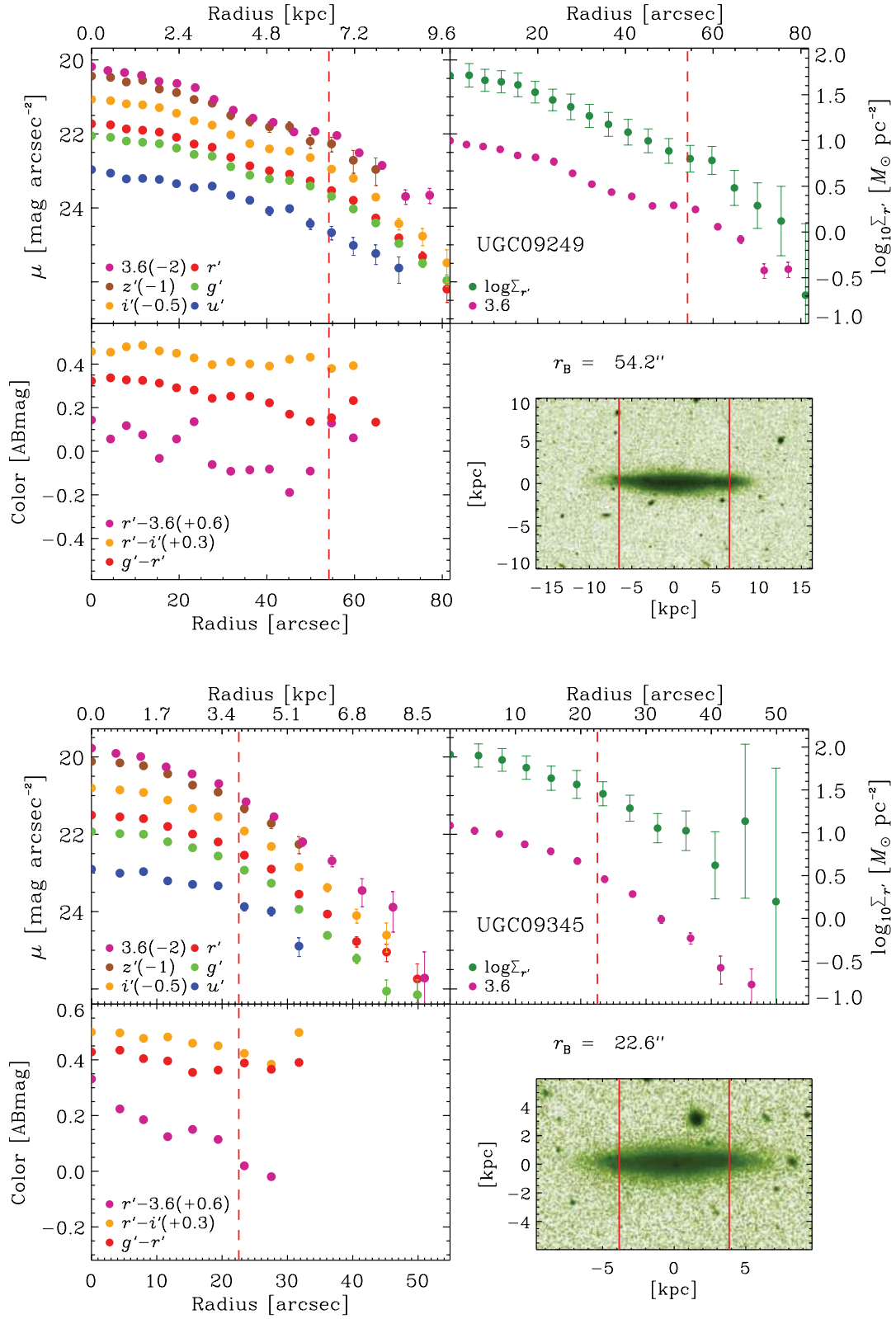
Figure B1 – *continued*
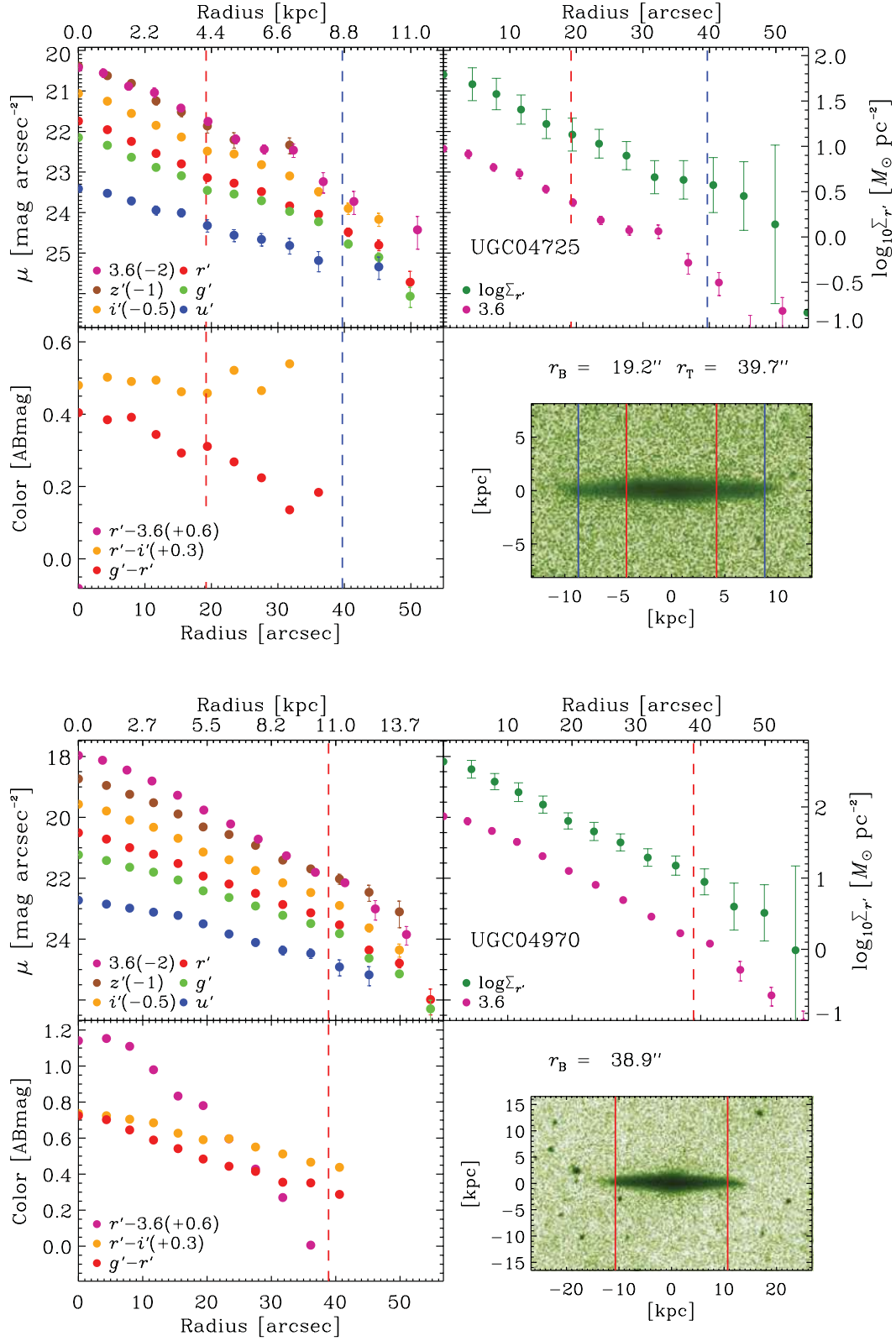
Figure B1 – *continued*
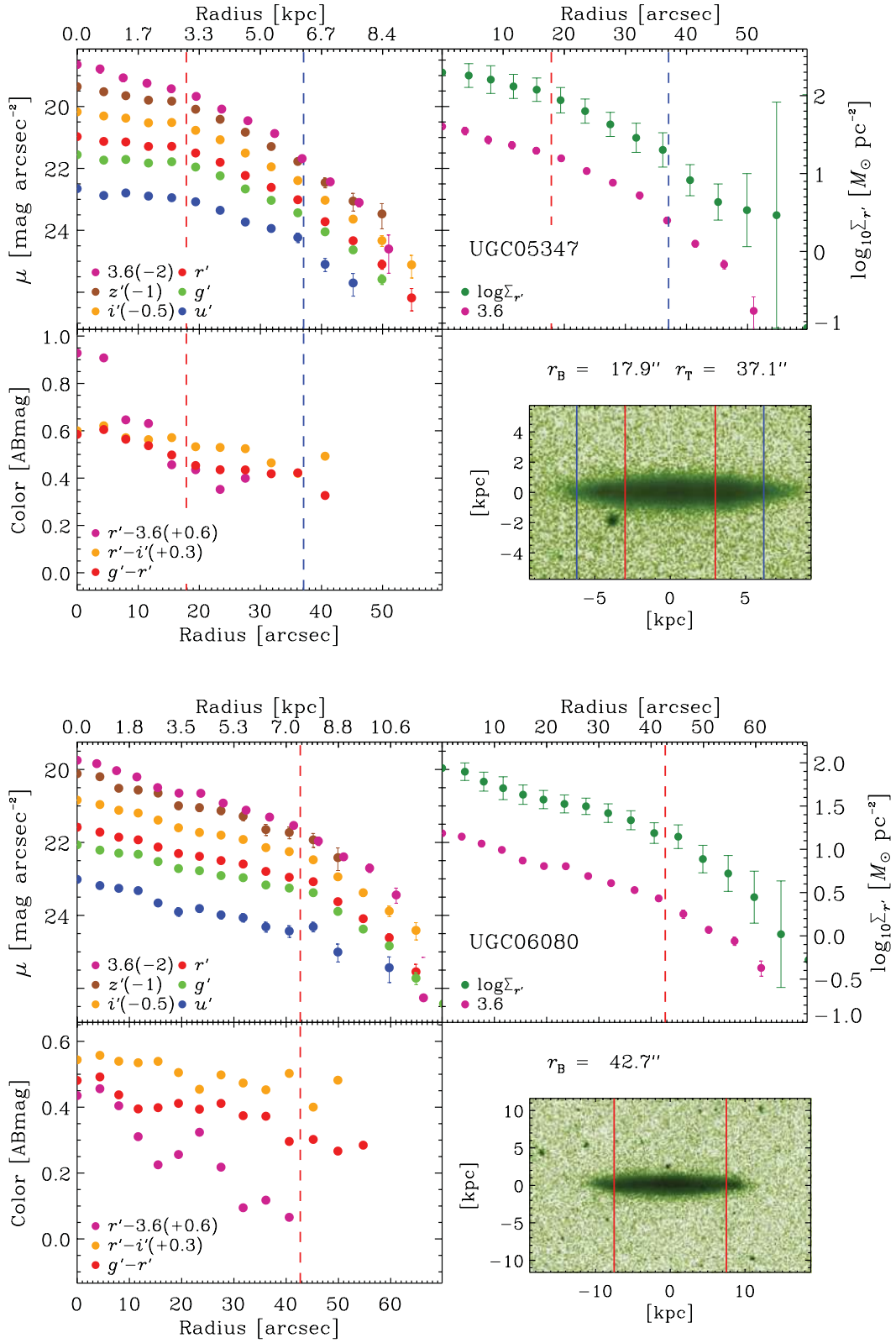
Figure B1 – *continued*
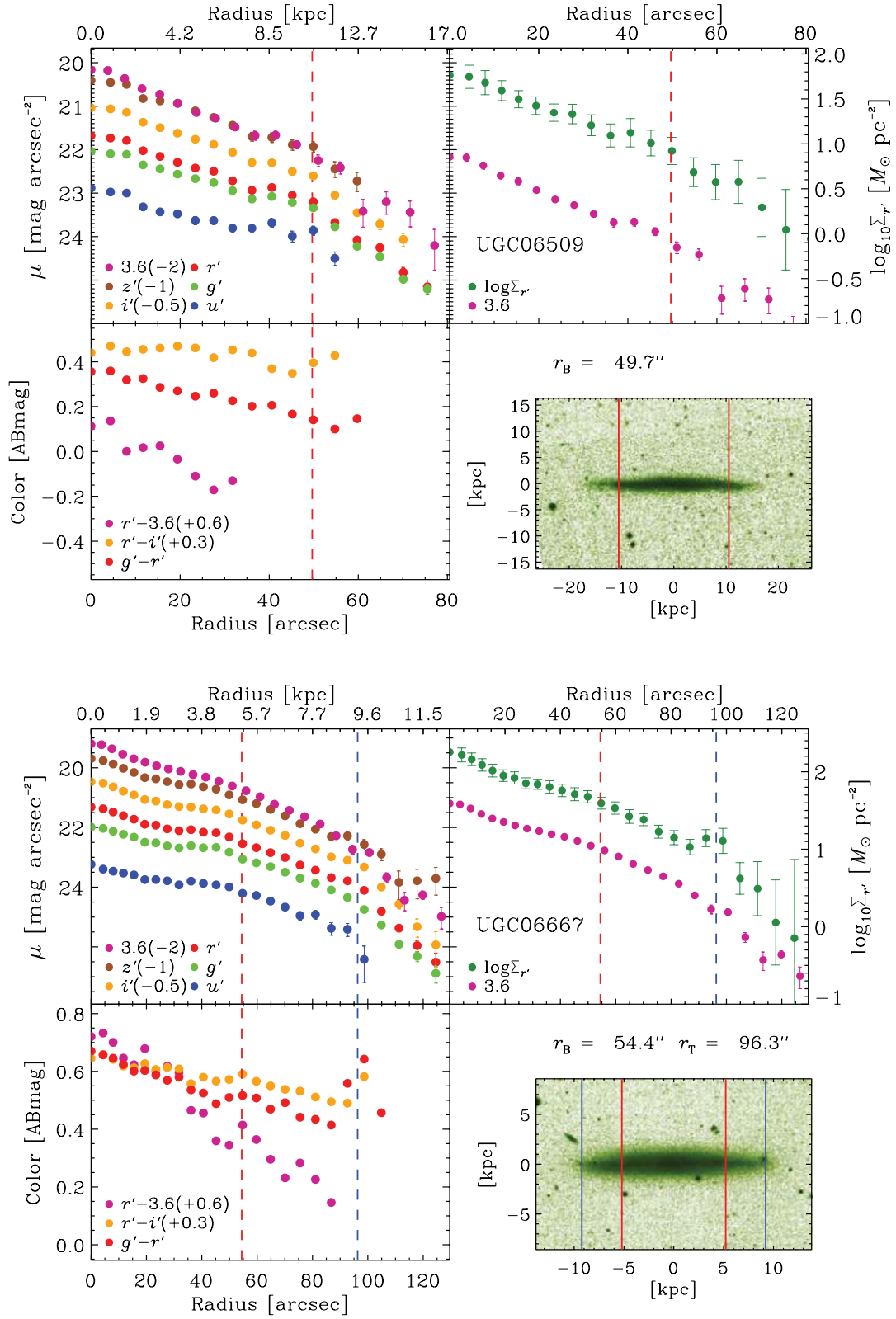
Figure B1 – *continued*
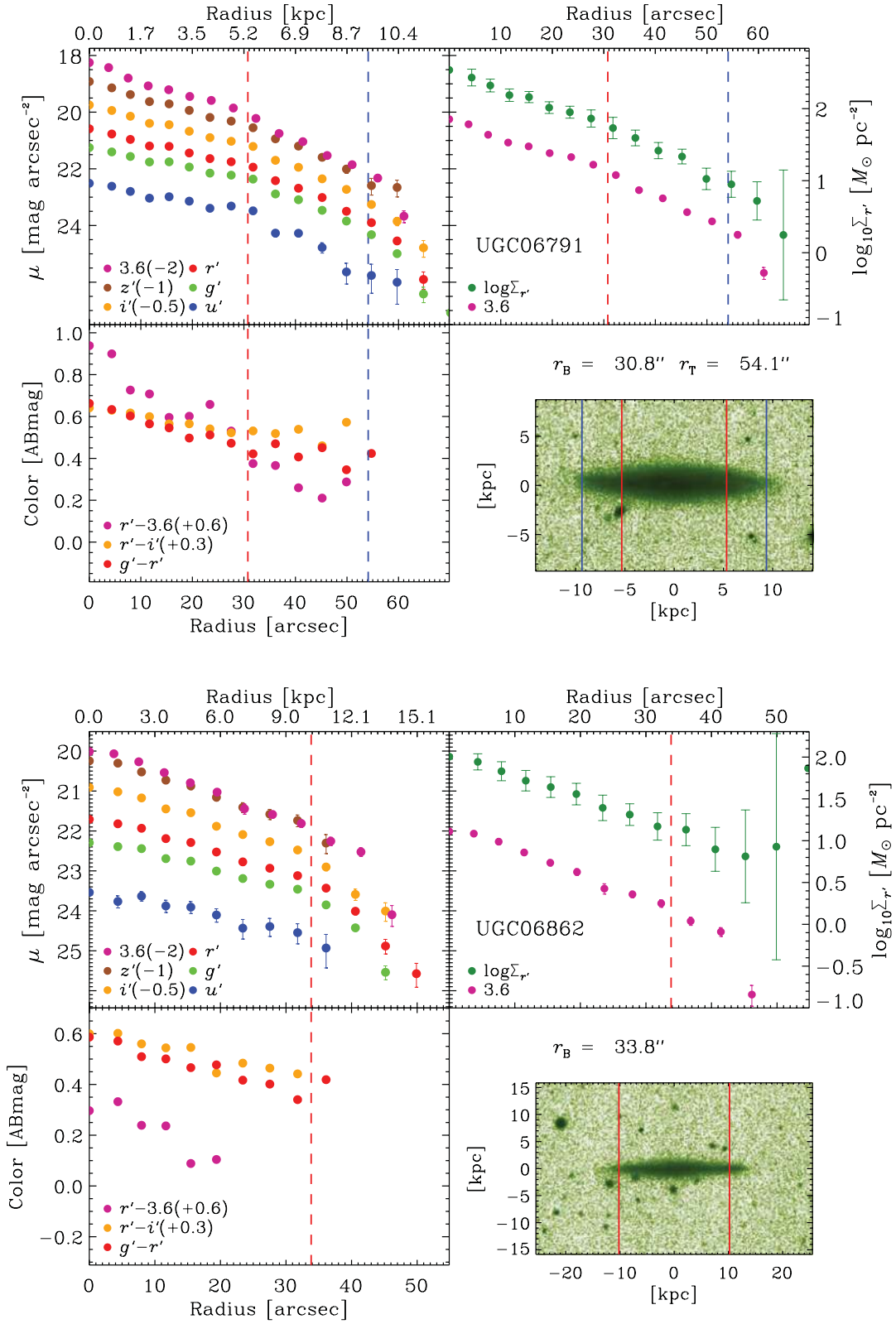
Figure B1 – *continued*
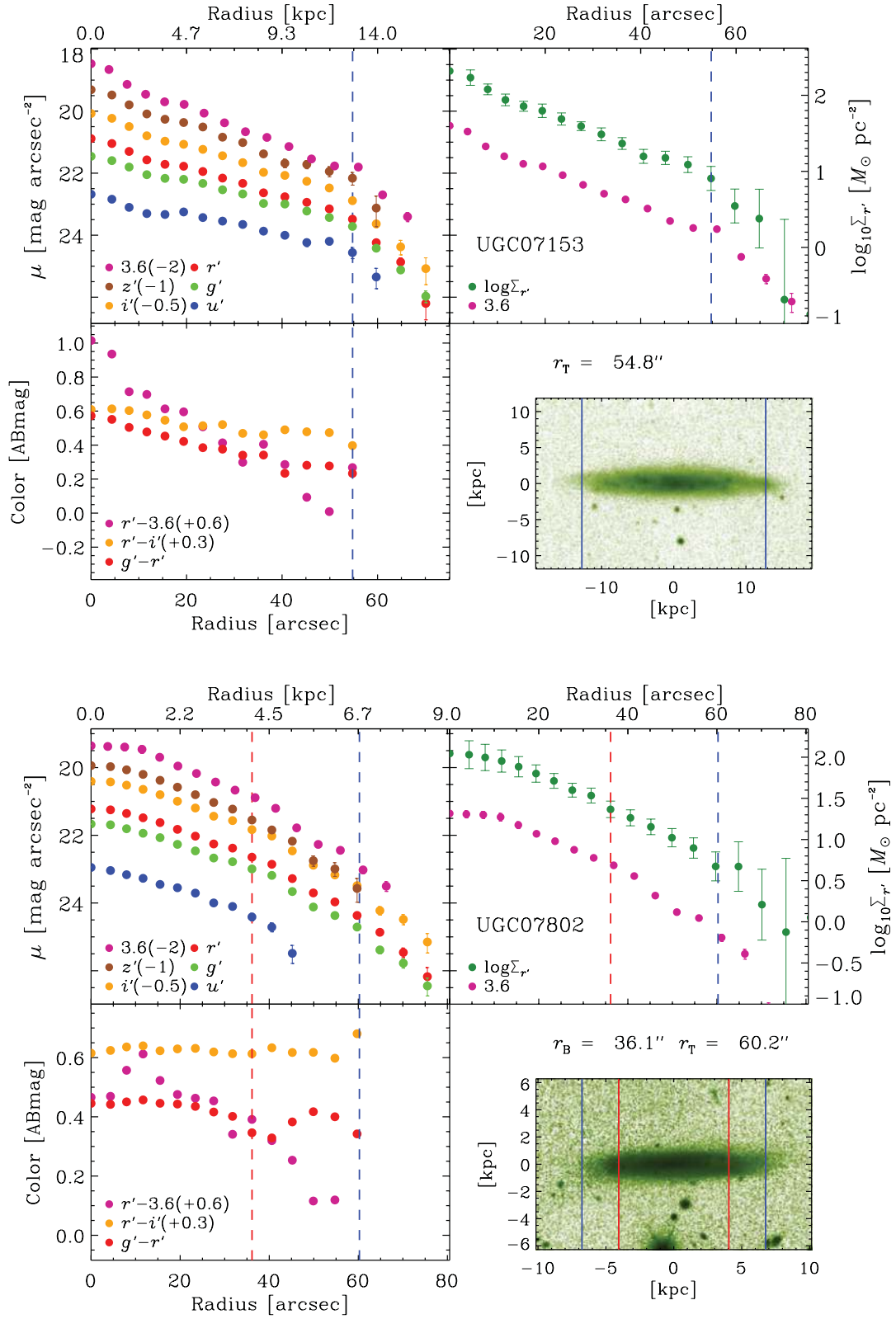
Figure B1 – *continued*

Figure B1 – *continued*

Figure B1 – *continued*

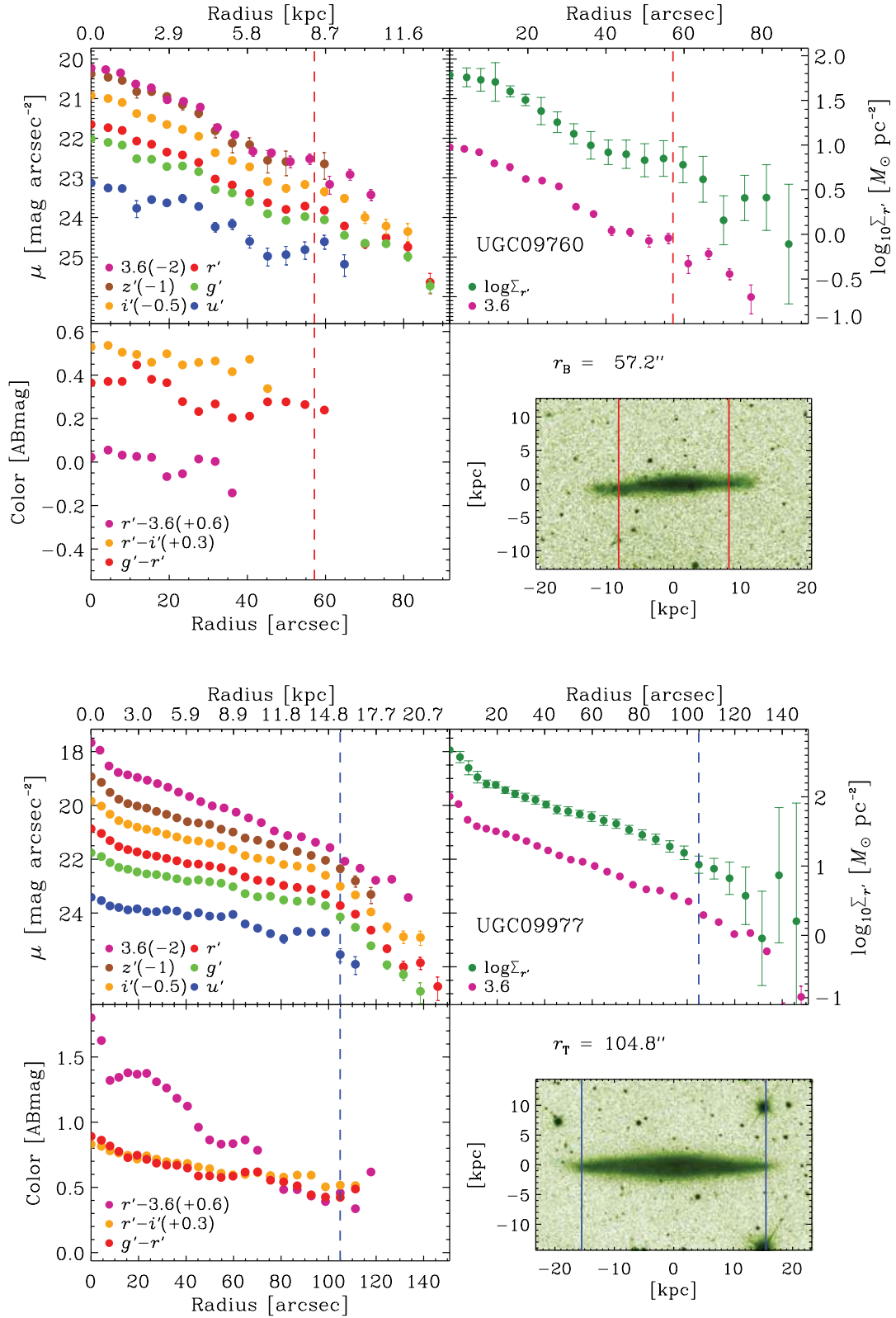**Figure B1** – *continued*
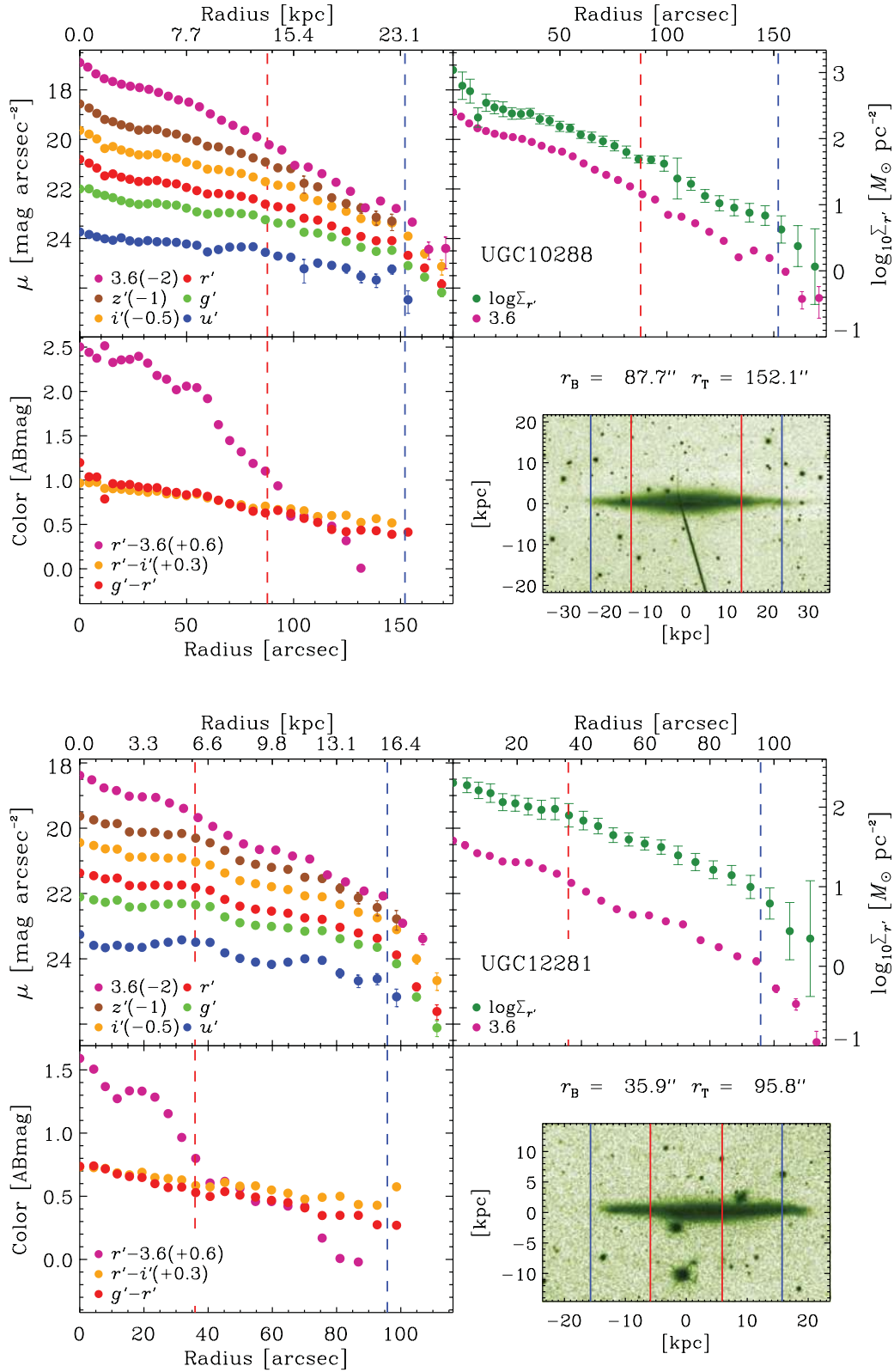
Figure B1 – *continued*

Figure B1 – *continued*

This paper has been typeset from a TEX/LATEX file prepared by the author.